Solid State Quantum Refrigeration

Hooman Mohseni

Northwestern University

March 2013
Final Report

DISTRIBUTION A: Approved for public release.

AIR FORCE RESEARCH LABORATORY
AF OFFICE OF SCIENTIFIC RESEARCH (AFOSR)
ARLINGTON, VIRGINIA 22203
AIR FORCE MATERIEL COMMAND

REPORT DOCUMENTATION PAGE

1. REPORT DATE (DD-MM-YYYY)	2. REPORT TYPE	3. DATES COVERED (From - To)
02/18/2013	Final Report	9/1/09-8/31/12

4. TITLE AND SUBTITLE

Solid-State Quantum Refrigeration

5a. CONTRACT NUMBER

FA 9550-09-1-0650

5b. GRANT NUMBER

5c. PROGRAM ELEMENT NUMBER

6. AUTHOR(S)

Mohseni, Hooman.

5d. PROJECT NUMBER

5e. TASK NUMBER

5f. WORK UNIT NUMBER

7. PERFORMING ORGANIZATION NAME(S) AND ADDRESS(ES)

Northwestern University
633 Clark St
Evanston, IL 60208-1110

8. PERFORMING ORGANIZATION REPORT NUMBER

9. SPONSORING/MONITORING AGENCY NAME(S) AND ADDRESS(ES)

AFOSR
875 N Randolph St
Arlington, VA 22203

10. SPONSOR/MONITOR'S ACRONYM(S)

11. SPONSOR/MONITOR'S REPORT NUMBER(S)

AFRL-OSR-VA-TR-2013-0117

12. DISTRIBUTION/AVAILABILITY STATEMENT

Approved for public release, distribution unlimited.

13. SUPPLEMENTARY NOTES

14. ABSTRACT

In this project, we investigated a new method, adiabatic quantum cooling, to address issues involved in semiconductor laser cooling. We have developed the theoretical framework, as well as numerical modeling methods to design and model semiconductor devices. We also grew several epitaxial structures with record blue-shift, and process them into suspended ridge structures. A novel processing method is developed that can achieve record high thermal isolation. In order to measure temperature accurately, both micro-thermistor and micro-thermocouple devices were integrated on the chip. We also developed a thermoreflectance temperature mapping system with ~300 nm resolution. Achieved temperature sensitivity was about 10 mK. We observe strong cooling component, although we have not achieve net cooling yet. Methods to increase the laser cooling beyond heating power are identified.

15. SUBJECT TERMS

Laser cooling, semiconductors,

16. SECURITY CLASSIFICATION OF:

a. REPORT	b. ABSTRACT	c. THIS PAGE
U	U	U

17. LIMITATION OF ABSTRACT

UUU

18. NUMBER OF PAGES

19a. NAME OF RESPONSIBLE PERSON

ONRRO

19b. TELEPHONE NUMBER (Include area code)

Final Technical Report

Name of Grantee: Northwestern University

Grant Title: Solid-State Quantum Refrigeration

Grant #:   FA9550-09-1-0650

Report Recipient: Dr. James Hwang; James.Hwang@afosr.af.mil

Summary

Review of the previous activities: in this section, a review over the previous efforts in the area of anti-Stokes laser cooling of Materials is presented.. Due to some difficulties which will be discussed in this report, researches could not cool semiconductors using this method.

Theory: in this section we present our studies for investigation of anti-stokes optical refrigeration assisted by quantum confined stark effect (QSCE). We also refer to virtual absorption as one of the important mechanisms of light matter interaction for non resonant excitations.

Modeling: Due to the nature of laser refrigeration, it is only implementable in materials that can have a good luminescence under appropriate circumstances. For this purpose we focus on multiple quantum wells (MQWs) which are more prone to this kind of cooling. We use band deformation potential theory, K.P theory and Poisson equation to determine the self consistent band lineups and wave functions. The obtained absorption spectra have been utilized to design the structures. Optical mode simulations were done using commercial software in order to design single mode optical ridge waveguides. We included a cladding layer between the ridge and the active region in order to increase the ridge width. Also coupling and back reflection of the laser beam into the lens were calculated using a transfer matrix MATLAB code in order to determine the tilt angle of the ridge waveguide with respect to the cleavage plane.

MQW Design: The designs which demonstrate the blueshift of Photoluminescence (PL) by the photogenerated carriers are introduced. In this section the mechanisms which lead to the blueshift are explained. The results of the experimental growth of these structures are also presented and have been compared with theoretical calculations.

Thermometry: In this section different methods of thermometry are introduced and their applicability is discussed. Non contact optical thermometry techniques are discussed first. Then a brief description of thin film thermocouples and thermistors as the thermometers on top of the final device is presented. Advantages and drawbacks of each thermometry method are also addressed.

Experimental Setup: The measurement setup and the optical components and instruments are introduced in this part. They provide a highly stable setup which is reliable for sensitive measurements. The setup is capable of thermoreflectance measurements which gives us the ability to get a map of temperature on the surface of the device.

Fabrication: In order to have a device which is best suited for the purpose of laser cooling and is sensitive enough for measurement of ultra low cooling powers, we introduce new processing designs and our efforts to realize them. One of them is the substrate etching and the other one is the idea of suspended waveguide. Process flow for each method followed by the thermal and mechanical stability of the final device is presented. The challenges of the processing are also addressed and the corresponding solutions are proposed. In this respect we preferred to make suspended waveguides to fulfill the necessary requirements of a suitable device prone to optical refrigeration. Using the transfer matrix code the scattering due to the change of the width of the waveguides was calculated and shown to be negligible. SEM photos of the final device indicated that the entire fabrication was successful. In order to increase the PL extraction, 1D grating was fabricated using Focused Ion Beam milling (FIB).

Measurements: A series of optical measurements were preformed on the fabricated suspended devices. In the first attempts the optical properties of the suspended waveguide were characterized by coupling from the side to the cleaved ridge. Then the temperature was measured using the fabricated thermocouples and the thermoreflectance setup. The temperature accuracy of thermocouple was 10^{-3}K which allows us to measure the change of temperature even for top illumination ridge using the Lock-in technique. The measurements show an increase of temperature by pump illumination but the temperature rise is lower for shorter wavelengths which have a higher absorption inside the quantum wells. This has been also confirmed by thermo reflectance thermometry. We then proceeded to do PL measurement on the device and determined the PL reabsorption coefficient. This coefficient is useful in order to determine the recombination coefficient rates and light extraction coefficient in future. Lastly a grating structure was designed to reduce PL trapping inside the material and was tested by focusing a tunable laser beam. The far field image of the scattered light shows that the direction of the diffracted beam is dependent on wavelength.

Conclusions and suggested future directions: in this section the general guidelines for future activities are presented. We have concluded that the top illumination doesn't introduce multimode complications and is easier to implement when the sample is inside the cryostat. The grating on top of the suspended structure helps the coupling of the pump beam into the suspended device and the extraction of the PL from the material. Both of the aforementioned consequences help optical refrigeration. Therefore new methods of testing the grating are proposed and going to be performed in future. Finally an excitation dependent PL method is proposed which can give the recombination coefficients of the material without the need for time resolved spectroscopy.

Review of the previous activities:

- In recent years, Researchers have considered the anti-Stokes fluorescence phenomenon as a mechanism for optical refrigeration of semiconductors. The general idea is as follows: a laser beam illuminates the sample and produces electron-hole pairs. These pairs undergo phonon absorption and recombine. Consequently photons with higher energies are produced which extract the energy of lattice vibration and as a result the material cools down. The first observation of such a phenomenon was not realized experimentally until 1995, in trivalent ytterbium ion doped heavy-metal-fluoride glass [1]. In rare earth ions, the optical 4*f* levels are shielded from the surrounding by the filled 5*s* and 5*p* shells, leading to the suppression of the multiphonon relaxation and are favorable for laser cooling [2]. However semiconductors have not been cooled yet using this technique. This is primarily due to reabosrption of the emitted photons and is referred to as luminescence trapping.

- Joule heating due to tunneling and thermionic emission current as well as other heat producing mechanisms in semiconductors such as Auger recombination, Shockley reed hall recombination and surface recombination can also prevent optical refrigeration. In order to achieve the cooling these phenomena should be suppressed. For a given material, the parameters *B* (radiative recombination coefficient) and *C* (Auger recombination coefficient) are fixed and can only be altered by varying the temperature of the sample. The other non-radiative recombination rate (*A*) includes surface recombination rate and Shockley Reed Hall recombination due to the impurities.

- Surface recombination depends on the quality of interfaces of the heterostructure. This quality is affected by the growth technique, environment, purity and thickness of the cooling material. For instance among all growth techniques for GaAs/GaInP double heterostructures, MOCVD method leads to the lowest surface recombination rates [3]. It is always desirable to passivate the surface of the device in order to reduce the dangling bonds and surface recombination rate.

- The Shockley Reed Hall recombination is lower for high quality grown MQWs which are optimally fabricated into final devices and contain lower levels of impurities and defects.

- Various ideas have been proposed to increase the photon extraction efficiency from the material and resolve the problem of luminescence trapping. For example when GaAs is a cooling target, it can be sandwiched between two GaInP layers which serve as an intermediate index matching material to reduce the luminescence trapping and

increase the extraction efficiency [4]. Two structures shown in Figure 1 are used to enhance the extraction efficiency of the aforementioned heterostructure: Texturing of the bottom surface leads to the randomization of photon trajectories, which results in a statistically larger number of photons to hit the surface at angles smaller than the critical angle and escape. The trade off is the red shift of the luminescence since only lower energy photons can travel relatively long distances and eventually escape before being absorbed [3]. When a dome lens which is broad-band antireflection coated at the photoluminescence energy is used as shown in Figure 1, isotropically emitted photons pass into the dome and reach its surface at nearly normal incidence. Obviously these rays can escape out of the material [3-, 4-]. Candidate lens materials are ZnSe and particularly ZnS which have acceptable transmission and refractive index close to that of GaAs [3]. The problem is that interface recombination is increased after the lift-off processing for attaching the lens since the quality of the surface is affected in this process. Therefore there is a tradeoff between the extraction efficiency enhancement and the internal quantum efficiency [5]. A sub-micron vacuum gap between the heterostructure and the absorbing substrate such as silicon allows the escape of photons without thermally perturbing the sample. This concept is depicted in Figure 2. If the gap space is less than 100 nm, luminescence rays of any angle relative to the surface can couple to the absorbing substrate via evanescent waves. Hence optical energy is transferred to the absorber which is in thermal isolation from the heterostructure due to the presence of the vacuum gap [3].

- Cooling efficiency is proportional to the ratio of the power of the emitted light to that of the absorbed light. By modifying the dependency of the radiative rate (R) versus the energy of the emitted photons, the cooling efficiency can be enhanced. In this sense, R should have a step like character. It should be negligible near and below the
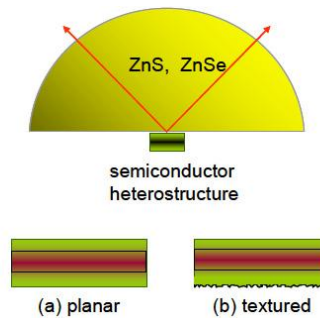

Figure 1. Two possible structures that use a high-index dome for increasing luminescence escape efficiency: (a) polished planar, and (b) surface textured heterostructures [3].
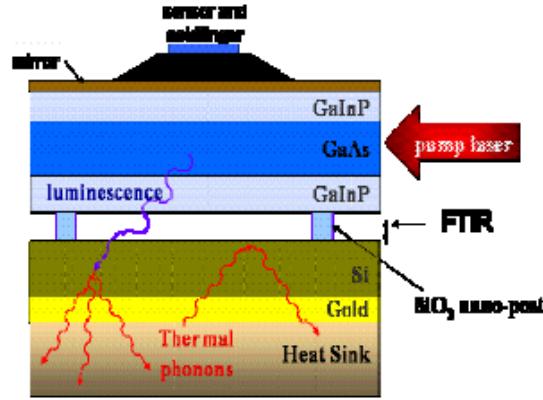
Figure 2. The concept of "nanogap": luminescence couples through nanogap; the vacuum nanogap maintains a thermal barrier [3].

energy of the absorbed photons and should be large a few *kT* above that energy. For this purpose all three components of R namely the density of electronic states, density of photonic states and the matrix element of transition should be modified as outlined below.

- Density of electronic states can be modified by means of impurity bands. The idea is shown in Figure 3, Here if the absorption takes place from acceptor to donor state, while radiative recombination takes place between the band edges the cooling efficiency will be increased [6-]. The main challenge is to assure that most of the photogenerated carriers get ionized into the conduction and valence bands while the absorption is still sufficient. For this reason the doping density and binding energies of donors and acceptors which are the main parameters at hand have to be carefully calculated [6]. As the binding energy increases the quantum efficiency first increases. But very large binding energy makes the ionization of electrons and holes very difficult and the donor acceptor pair recombination becomes dominant and quantum efficiency quickly drops.
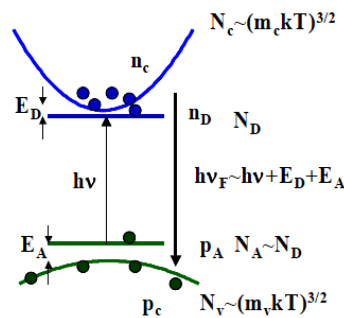

Figure 3. Principle of bandgap engineering for laser cooling using doping states. E_A and E_D denote acceptor and donor binding energy [6].

- Density of photonic states can be modified in photonic bandgap structures or by using surface plasmons. By carefully designing photonic bandgap in the vicinity of band edge transition of semiconductor the emission at lower energies becomes forbidden and has to take place at higher energies [6-]. In order to allow the absorption of the input light a "defect band" can be used. It acts as a "waveguide" for propagation of the pump light. It should be noted that the overall radiative recombination rate should not be decreased to the point where nonradiative recombination prevents optical refrigeration. By carefully selecting photonic band edge, the cooling efficiency can be enhanced by the factor of two or three [6-]. It is also shown that the energy transfer from the semiconductor to the metal is enhanced using the excitation of surface plasmon polaritons (SPP) and their subsequent decay in the metal [6].The idea is shown in Figure 4. The semiconductor which is GaN is coupled to the heat sink which is covered with a layer of an SPP supporting metal (Ag). In this combination, surface plasmon resonance happens at 3.6 eV, which is very close to the energy gap of GaN (3.47 eV). A thin layer of a wider band gap material (AlN in this example) is employed to reduce the surface recombination rate. When the thickness of this layer denoted by t_{gap} is much smaller than the wavelength in vacuum, an SPP mode that spreads into the semiconductor can be supported. Near the plasmon resonance frequency, the dielectric constants of the metal and dielectric have equal magnitude but opposite sign. As the frequency reaches the resonance frequency, the field gets more and more confined at the interface. The density of SPP states increases significantly near energy of resonance, and that leads to the enhancement of the spontaneous emission into the SPPs. Then the energy of the spontaneous emission should be coupled from the high density SPP modes into the low-density radiation modes. The overall radiation efficiency of SPPs is still low considering the nonradiative decays of SSPs, but fortunately non radiative decay of SPP and producing phonons happens inside the metal which is thermally isolated from the semiconductor. Therefore the semiconductor can be cooled down if the resonance of the SSP is adjusted a few kT above the band gap energy of the semiconductor.
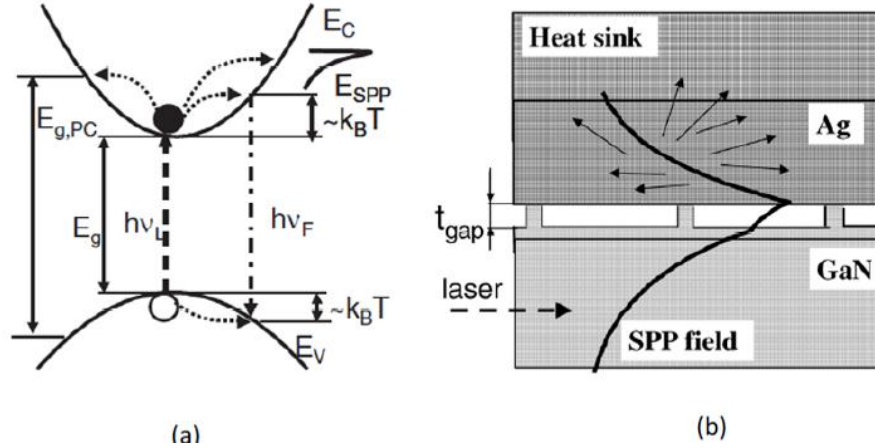
Figure 4. (a) Basics of laser cooling of a semiconductor using a photonic band gap with energy or an SPP. (b) SPP-assisted cooling [6].

- Finally, Matrix element of transition (oscillator strength) can be modified using novel structures which are the main subject of this report. We propose the use of quantum confined stark shift as a method to blueshift the spectra of Matrix element of transition by means of the photogenerated carriers.

Theory:

- In order to facilitate the laser refrigeration of semiconductors, we seek to use quantum confined Stark effect in order to increase the bandgap after the generation of electron-hole pairs. In this way the emitted photons are guaranteed to have a higher energy than the absorbed ones and also the chance of reabsorption decreases because as the photons are escaping the bandgap is continually increasing.

- The increase of energy level difference of electrons and holes due to quantum stark effect happens due to the screening of the internal field by the photogenerated carriers. The band deformation caused by photogenerated carriers in asymmetric type-II quantum wells has the same origin. It is evident that this phenomenon results to blueshifted PL and cooling but the physical interoperation of the energy transfer in this process is still under investigation. In this section we present the most relevant articles which may reveal the physics behind this phenomenon in near future.

- The first question that comes to mind is the location of the electrons and holes immediately after creation. According to Refs [**Error! Reference source not found.**, 7] in which the dynamics solution of self consistent Poisson and Schrödinger equations in presented, the electron hole pairs immediately occupy the empty wavefunctions (wavefunctions calculated without the presence of photogenerated carriers) therefore the screening immediately happens but it decreases over time until

the self consistent state is reached. The band gap increases immediately upon creation of electron hole pairs and the origin of this energy shiftin one of our research topics.

- We first assumed that the energy level broadening due to phonon scattering is negligible and the anti stokes process is absent. In this case virtual carriers are created by absorption of virtual photons [9, 10]. The rate of creation of virtual carriers is proportional to the detuning which is the difference between the energy of the photons and the bandgap[9].

- Although virtual carriers don't exist but they can induce electric field [9, 10,11], therefore our first concern was to see if a considerable density of virtual carriers are produced sooner than real carriers. If virtual carriers can screen the internal electric field and increase the bandgap before real absorption happens then QSCE induced laser refrigeration becomes out of question. For this reason we calculated the absorption of virtual photons according to Ref [9]. The absorption of virtual photons is negligible compared to the real photons based on our simulation. However the study of virtual excitation can enlighten the physics of laser refrigeration assisted by quantum confined stark effect. In fact light shift in presence of dressed states, two photon absorption and virtual photon absorption should have the same physical origin [12] and are important mechanisms in off resonance light matter interactions.

- It has been previously shown that absorption of virtual photons can lead to joule heating in the external circuit used for biasing the MQW [11]. The energy comes from the photons which are redshifted after passing the MQW region [11]. We are trying to demonstrate that the reverse process can happen under certain circumstances and the lattice can be cooled down.

Modeling

- Modeling of the MQW structure is divided into three parts: Quantum mechanical simulation of absorption spectra, simulation of optical modes coupled into the ridge waveguide and the simulation of carrier lifetimes and Quasi-Fermi level profile inside the device.

- We developed a software which is based on K.p method and includes Poisson self consistent potential solver to account for large photogenerated carrier densities. The

excitonic effect was calculated based on a variational method and the band lineups in presence of strain are estimated using the well known "model-solid theory" [13]. The developed software is able to automatically include the mixed interface layers and to calculate the total strain of a period of the MQW structure. Furthermore, the user can define the mesh of the Poisson solver arbitrarily in order to increase the self-consistency between the Schrodinger and Poisson equations. The resulting absorption spectra are used to estimate the energy blueshift which is necessary for designing the optimum structure. The photoluminescence was also simulated by the software and showed an excellent agreement with experimental results for Sb free quantum wells as shown in Figure 5.

- To maximize the energy extraction efficiency, the bimolecular radiative recombination rate should be dominant over the nonradiative recombination rates and carrier escape rate due to tunneling and thermionic emission current. Tunneling and thermionic emission are mechanisms which are responsible for the carriers' escape out of the quantum well and should be suppressed. The software was so devised that it can calculate the thermionic and tunneling current for all bands and with any barrier shape. It should be noted that by calculating the carrier lifetime due to different recombination mechanisms and the carrier escape rate due to tunneling and thermionic emission, it is possible to calculate the steady state carrier density inside the quantum wells. Knowledge of the steady state carrier density is necessary for the calculation of the quasi Fermi levels and the self consistent potential.

- Optical simulations have been done by Lumerical which is a commercial field simulator. We assumed an average refractive index for the active layer of the waveguide. We have determined the ridge width to be 5 µm so that only the first mode is effectively coupled to the active region. This is beneficial since it eliminates the confusion regarding mode mixing effects. Otherwise the change of temperature and correspondingly the refractive index can change the coupling of the different modes and may lead to a misinterpretation of absorption coefficient. On the other hand, in presence of different modes, the internal reflection inside the modulator leads to a beating effect and large oscillation of output power and makes the output power unstable. The result of the Lumerical simulation has been presented in Figure 6.

- In order to increase the maximum width of the waveguide for single mode operation, the change of the effective dielectric constant of the active region seen by an optical beam along the x direction as shown in Figure 6 must be decreased. For this reason
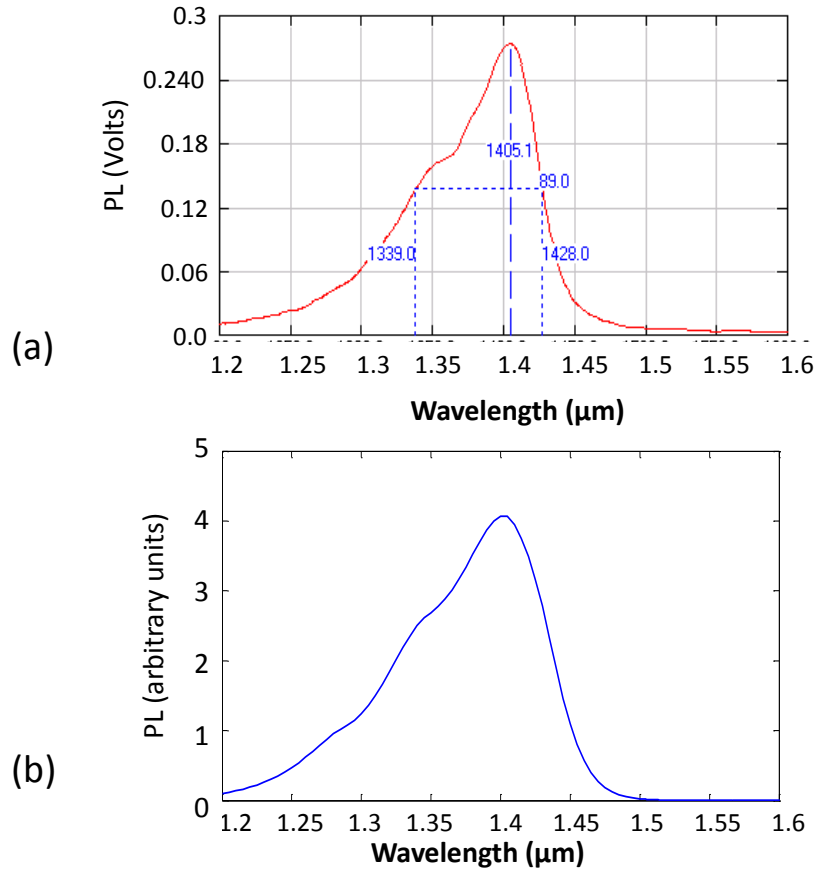
(a)

(b)

Figure 5. (a) the experimental photoluminescence at the center of the wafer as measured by photodetector and expressed by units of volt (b) theoretical photoluminescence calculation assuming the photogenerated carrier density is equal to 5×10^{17} cm^{-3}. This result is in good agreement with the experimental data.

another p-doped InP layer was included to make the effective dielectric constant of the part of the active region under the ridge closer to that of the other parts. The appropriate dimensions of the ridge turned out to be 5 μm × 2 mm which can be easily fabricated by conventional photolithography methods. The corresponding mask was designed and ordered.

(a)

(b)
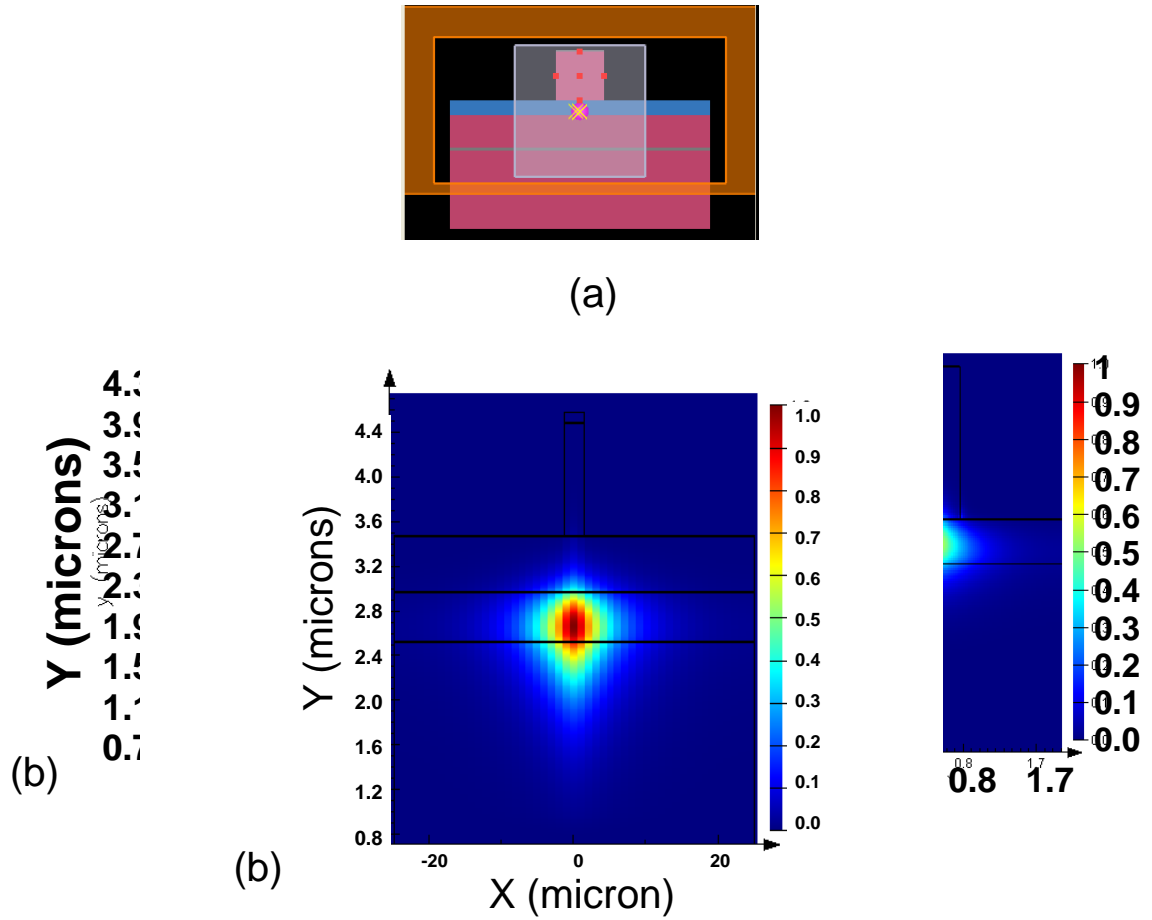
Figure 6. (a) Cross section of the ridge waveguide which is simulated by Lumerical. The layer specifications from bottom to top is as follows: 1- n-doped InP substrate, 2- 100 nm of InGaAs absorbing layer, 3-1.5 μm of gradually n-doped InP bottom cladding layer, 4- active layer which is 300 nm thick, 5- 0.5 μm of p-doped InP top cladding region, 6- 15 nm of InGaAsP as an each stop layer, 7- 1 μm of gradually p-doped InP which serves as the ridge, 8- Top contact.(b) the intensity profile of the first mode.

- In order to see how much of laser is coupled into the ridge and how much is reflected at the input and output facets, a MATLAB program was devised based on transfer matrix method and Fresnel reflection and transmission formulas for reflection of s-polarized and p-polarized light. The inputs of the programs are the layers' widths and effective indices, polarization and angle of the beam for the case of finding transmission and reflection coefficients. This program is also cable of mode simulations for a given structure. The user can define the mesh and effective index accuracy for the mode simulations using this program in order to have best results in a short time.

- Using the developed code describe above, the simulation of the cone of focused light incident on the structure is explained. . shows that a cone of light is focused
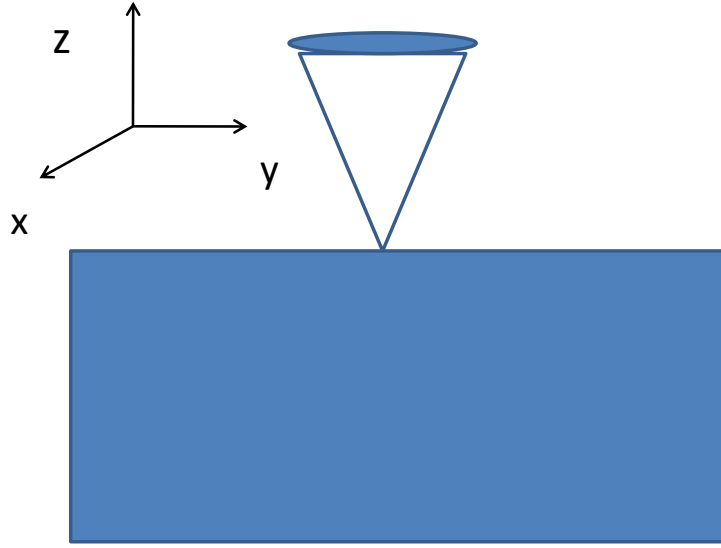
Figure 7. schematic of the structure used for simulation.

- on the MQW region from the top view so that "$\hat{x}$" is the unit vector orthogonal to the MQW layers. when the electromagnetic field is TE, i.e its electric field (E) is parallel to quantum well layers, it can be described as:

$$E = A(\theta)e^{ikr}(\hat{r} \times \hat{x}) \tag{1}$$

In the above equation A is the amplitude which has a Gaussian relation with respect to θ. Θ is the azimuth angle with respect to the z axis. k is the wavevector and r is radial position. It should be noted that for a specific angle of incidence, the Cartesian axis as shown in . should be rotated by the angle of incidence around the x axis. "$\hat{r}$" and "$\hat{x}$" in the above equation are the unit vectors of the spherical and Cartesian coordinates respectively. The above equation can be further simplified to:

$$E = A(\theta)e^{ikr}(\cos(\theta)\hat{y} - \sin(\theta)\sin(\varphi)\hat{z}) \tag{2}$$

In which y and z are the unit vectors. The both terms on the right side of the above equation are TE modes; however the first term is p-polarized while the second one is s-polarized. For any arbitrary cone with a well definite angle of incidence, each ray with a definite θ and φ is considered and its electric field is calculated according to the above equation, the Euler transformation is made to express its electric field in terms of unit vectors in the original Cartesian coordinate defined in Figure 7. Then its TE and TM parts are separated and transmission and reflection coefficient are calculated using the transfer matrix method. The transmitted TE energy then is

calculated and is sent to the stock of the transmitted energies of the cone under consideration. The angle of the reflected beam is calculated and if it is within the incident cone, then the reflection energy for both TE and TM part of the ray will be sent to the stock of the reflected energies of the rays. The restriction imposed on the angle of reflection ensures that only the portion of the reflected beam coupled back to the lens is considered. Once the above procedure is done for all rays of the cone the then the TE coupled energy ratio for the cone is calculated by dividing the stock of the coupled TE energy of the rays to the total energy of the rays forming the incident cone. The same division is done for finding the percentage of back coupled light.

- The correct angle was determined for which a good coupling into the tilted ridge waveguide and a good reflection loss at the output facet back into the ridge and also a good back reflection loss into the lens. for the input facet of the ridge waveguide the simulations was done based on the method described in the previous paragraph whereas for the output facet the combination of transfer matrix and loss due to due the phase change of rays hitting the tilted output facet has been used [14, 15]. In all of the calculations the overlap loss of the lens spot and the mode spot has been neglected and assumed to be the same for all of the angles. The results of simulations are shown in Figure 8.

- The simulations show that the ridge should have angle between 5-7 degrees with respect to the cleavage plane. The ridges that are fabricated have angle of approximately 7 degrees with respect to the cleavage plane.
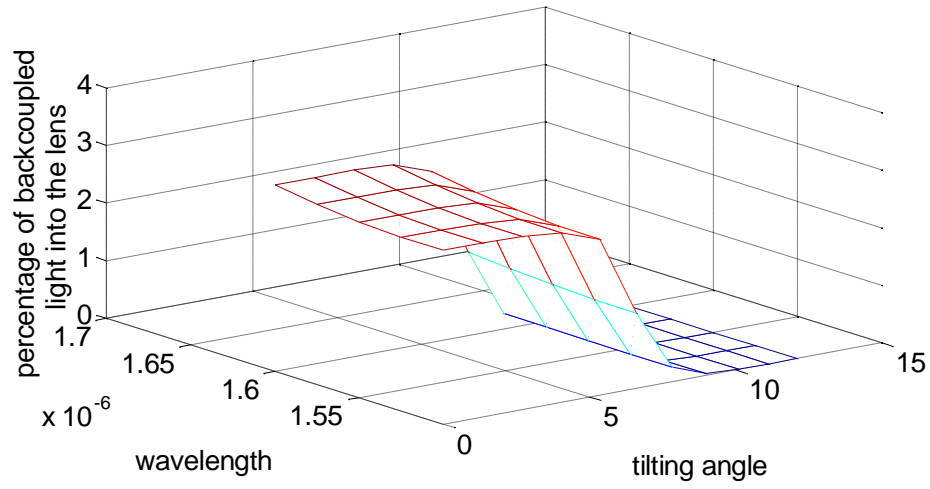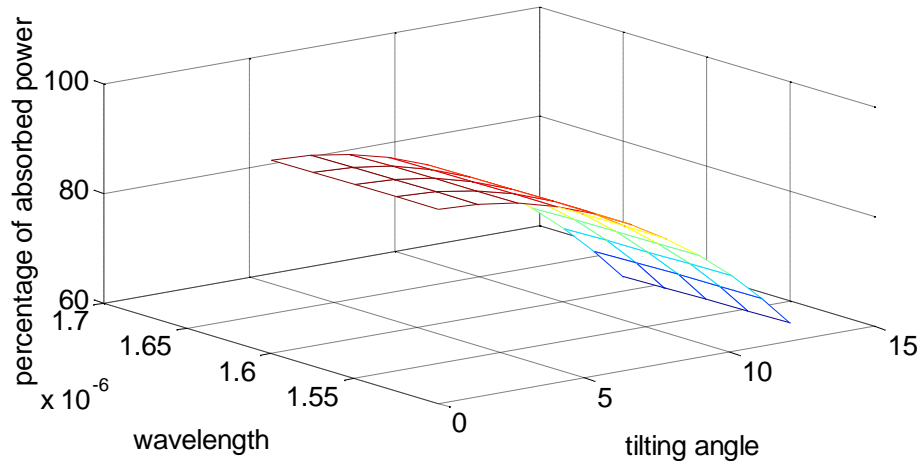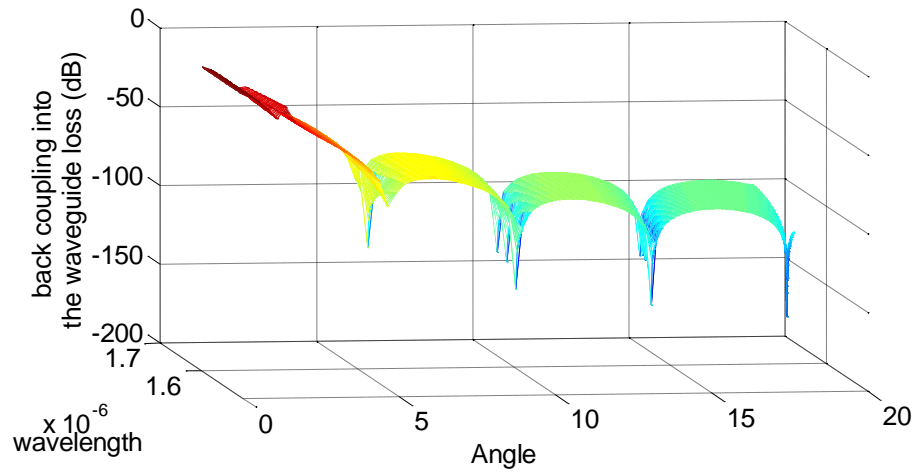
Figure 8. results of a) percentage of the backcouples light into the lens b) percentage of absorbed power c) back coupling loss into the ridge waveguide at the output facet versus the tilting angle (degrees) and wavelength (m)

MQW Design

- The transition energy within the quantum wells redshift as the total in-well electric field increases due to quantum confined Stark effect. We have exploited this phenomenon in all of our designs to get a blueshift as electron-hole pairs are generated.

- It has been shown that in strained quantum wells grown on (111B) substrates, the direction of the piezoelectric field is toward (111A) for compressively strained layers and (111B) for tensile ones [16, 17]. Therefore it is possible to have the piezoelectric field in opposite direction to the built in and reverse bias field [16]. As a consequence it is possible to tune the in-well electric field by changing the reverse bias. It is important to work in the reverse bias regime since in this case the electrical current is low and joule heating is not a major issue. Furthermore the carrier out-of-well escape rate can be kept much lower than the radiative recombination rate in reverse bias regime. The photogenerated electrons and holes shield the in-well electric field after being separated. Hence they increase the bandgap before recombination. In Figure 9 one period of such a MQW structure has been shown. Note that the presence of the photogenerated carriers flattens the QW and leads to a blueshift.

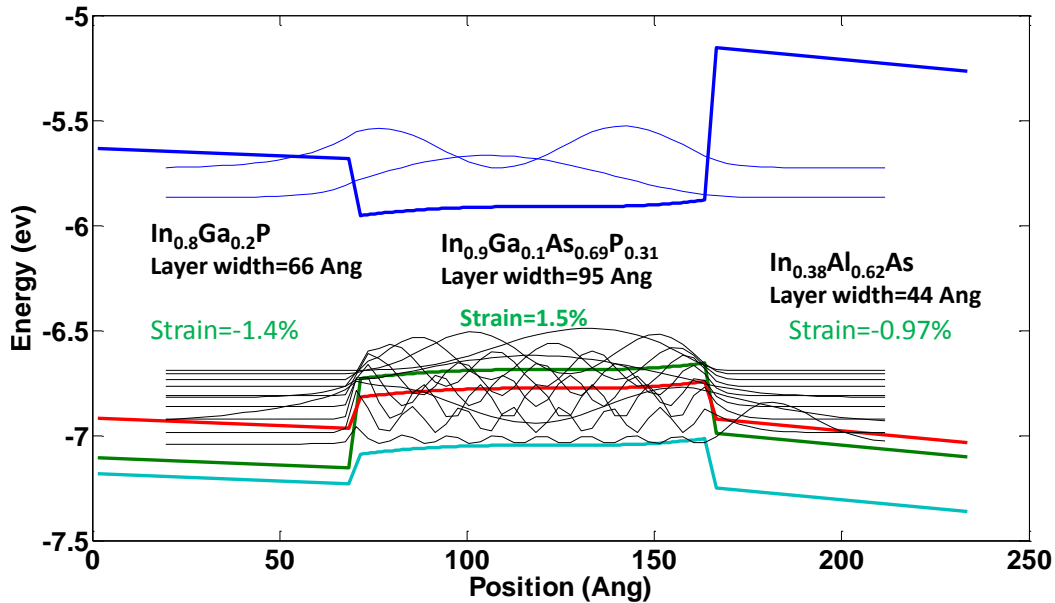- Figure 9 shows an optimized structure on a (111)B substrate based on our ed

Figure 9. The self consistent band diagram of one period of the MQW grown on the (111B) InP substrate. The wavefunctions were also shown. In this structure the wavelength at which the absorption is 100 cm^{-1} reduces from 1558 nm to 1540 nm when the density of the photogenerated carrier reaches 2×10^{20} cm^{-3} .

bottom and the internal piezoelectric field is from bottom to top. On the other hand we are interested in a compressively strained quantum well. So that the heavy hole band are pushed upwards in the band diagram and consequently the interband transition with the lowest energy occurs between the first heavy hole and the first electron level. This makes the absorption of the TE mode favorable when the sample is shined with a light of the lowest transition energy. The composition of the quaternary element was obtained by optimization of different parameters which are described below.

- The higher the piezoelectric field the higher would be the difference between the energy levels of the unscreened and the screened quantum well and the corresponding blueshift.

- Wider gap compositions allow for a wider quantum well. The dependence of the blueshift on the width of the quantum well is as follows: increasing the width of the quantum well first increases the blueshift due to the reduction of the overlap between the wavefunctions of the electrons and holes and prevents charge cancellation. But as the width increases further the electron subbands in the conduction band and the hole subbands in the valence band get closer together and the probability of the occupation of other subbands increases. Since higher order subbands have wavefunctions which are more evenly distributed along the width of the quantum well, a significant charge cancellation occurs and the self consistent results confirm that the blueshift decreases.

- As pointed out before, the tunneling and thermoionic emission should be suppressed. This can be only achieved using wide barriers with high conduction and valence band offsets for the quaternary material. Here we have used an asymmetric barrier scheme according to Figure 9. The reverse bias is in the opposite direction of the internal electric field and the external electric field is from right to left. Therefore electrons tend to move from left to right to constitute the output current. For this reason a tall barrier was used to block the electrons at the right of the quantum well. The opposite is true for the holes. However in the asymmetric structure there is no tall barrier for the electrons (holes) at the left (right) side of the quantum well. These short barriers do not affect the thermoionic and tunneling current but they increase the sensitivity of the self consistent solution of the Schrödinger equation to the amount of the in-well electric field. It has been shown that the proposed structure has the highest blueshift with lowest electrical current favorable for optical refrigeration. However the amount of blueshift is not sufficient and also reliable experimental values for the piezoelectric field of the compositions with high percentage of indium have not been reported in the literature. This is due to the growth problems of these compositions such as

indium segregation effect. These shortcomings made us to investigate other structures.

- Another idea is to use the step quantum well grown on (100) substrates as shown in Figure 10. In this case the laser is tuned to make transition between the energy levels of the narrow quantum well. The lowest energy level in the wide quantum well is separated by 30 meV from the energy level of the narrow quantum well. Since this value is near to the electron-phonon interaction energy in these materials, it is highly
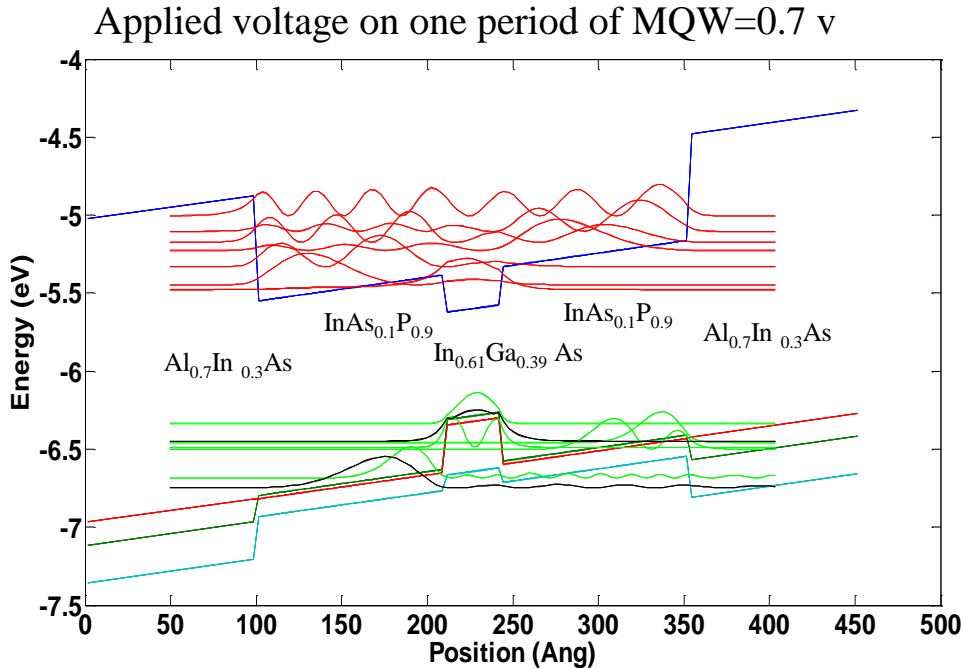
Applied voltage on one period of MQW=0.7 v

Figure 10. The self consistent band diagram of one period of the step MQW. The wave functions were also shown.

quantum well. If they recombine at these states, blueshift occurs and the semiconductor will be cooled down, otherwise if they are trapped again inside the narrow well before recombination, again we expect blueshift because the remaining carriers inside the wide well screen the electric field and increase the transition energy of the narrow well. The layers are strain balanced to ensure the high quality of fabrication.
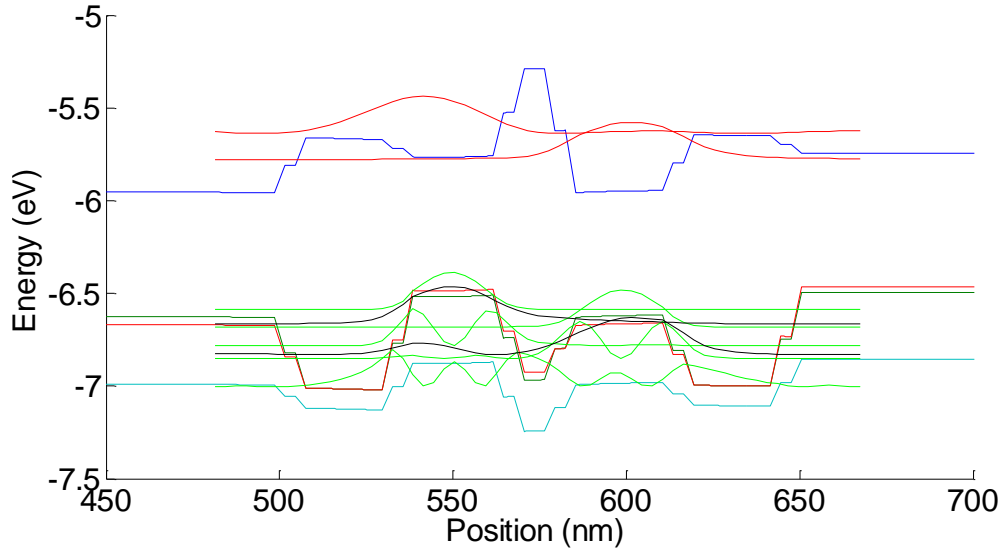
Figure 11. The self consistent band diagram of one period of sample VE1853 (see table 1 for its specifications) grown on the (100) InP substrate. The wavefunctions were also shown. In this structure the wavelength at which the absorption is 100 m^{-1} reduces from 1559 nm to 1553 nm when the density of the photogenerated carrier reaches 5×10^{17} cm^{-3} .

- Type-II transition also exhibits blueshift of photoluminescence which has been confirmed by many experiments [18]. As it is evident from Figure 11 the holes are generated in the GaAsSb layer. They provide a local positive charge in this layer and push down the valence and conduction band in this layer whereas electrons are generated inside the InGaAs layer and pull up the band diagram of that layer correspondingly. Therefore the consequent type-II recombination will emit photons with higher energies compared to the absorbed ones. The simulation result also verifies this conclusion. The InAlAs layer has been used as barrier layer to confine the electron and holes. In order to have a higher average refractive index within the active region and also to have higher oscillator strength, this layer should be thin enough. However a very thin InAlAs layer leads to a significant tunneling current that is undesirable.

- Due to the growth difficulties of the Sb based structures, we proposed several structures based on type-II transition. In all of the structures with specifications listed in tables 1 through 8. We determined the compositions and well widths to facilitate and test the growth procedure while having the maximum blueshift at a given density of photogenerated carriers. The determination of the blueshift due to quantum confined stark effect is according to the absorption spectra. After excitation the wavelength at which the absorption is 100 cm^{-1} is blueshifted and the value of this blueshift has been used as the criteria.

- Table 9 shows that the result of the experiments contradicts those of theoretical predictions for Sb containing quantum wells. We believe that this is due to the

material quality of the Sb used for the growth. In addition the anomalous behavior of Sb has been mentioned frequently in the literature and the exact band alignment of the $GaAs_ySb_{1-y}/InP$ is still unknown [19, 20]. Many experiments have revealed smaller band gap energies for GaAsSb than the theoretical calculations. The discrepancies $_{-y}Sb_y$ layers ergy [23].
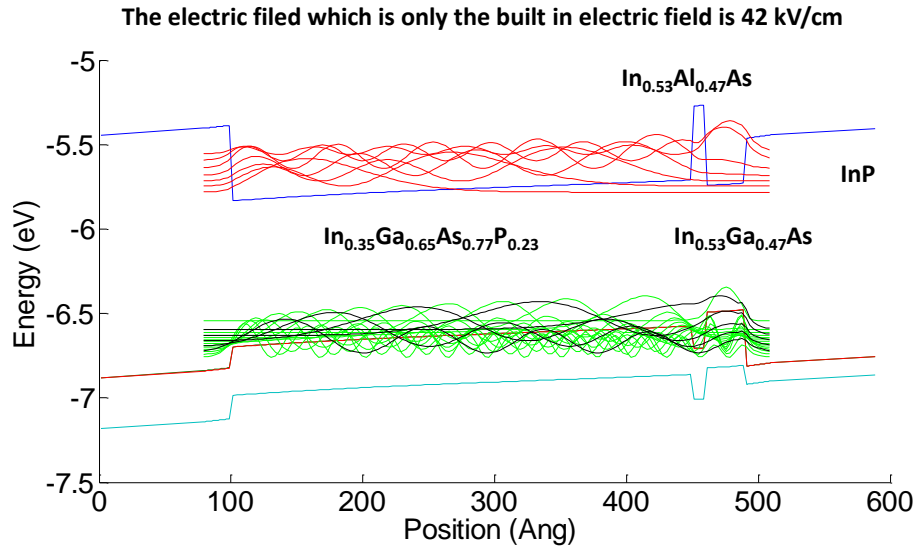
The electric filed which is only the built in electric field is 42 kV/cm

Figure 12. The band diagram of one period of VE1902 (see table 7 for its specifications) grown on the (100) InP substrate. The wavefunctions were also shown.

When the carrier concentration is 1e17 the quasi fermi level of the electron is below the First band

- Screening of the external electric field can be also used to blueshift the emission
  The blueshift of absorption (the criteria is the absorption of 10cm-1) is 5.6 mev
  spectra by the generation of carriers. One period of the designed structure has been shown in Figure 12. For the ease of the growth by MOCVD, only lattice matched layers were used in the design.

- Between all lattice matched quaternaries $In_{0.53}Ga_{0.47}As$ has the highest valence band energy offset with InP and is therefore suitable for reducing the hole current. The thin InAlAs modified the electron wavefunctions. First of all it increases the separation of electron levels. Second it increases the energy Eigen value of the electrons and therefore allowing for a wider InGaAsP well with higher value of blueshift. Moreover it improves the electron wavefunction shapes and removes the lobe of the first four electron levels inside the InGaAs and prevents the charge cancellation.

Epitaxial Growth:

- In the following, the structures of the grown structures are presented. In order to investigate different experimental parameters of the growth process, many of these structures have been grown just for calibration**.**

Table 1			Sample: VE1853 and VE1856[*]		
Layers of a Period	1	InP	2.5	undoped	Quantum well first layer
	2	$GaAs_{0.57}Sb_{0.43}$	2.6	undoped	Quantum well second layer
	3	$In_{0.45}Al_{0.55}As$	0.9	undoped	Quantum well third layer
	4	$In_{0.63}Ga_{0.37}As$	2.8	undoped	Quantum well fourth layer

- VE1856 has the same structure as VE1853, but in the growth procedure had an increased As flow compared to VE1853 to check that if the inconsistency between X-ray simulation and measurement of VE1853 was due to the lack of As. The measured and the simulated X-ray have been shown in Figure 13.

Table 2			Sample: VE1860		
Layers of a Period	1	InP	2.5	undoped	Quantum well first layer
	2	$GaAs_{0.765}Sb_{0.24}$	2.6	undoped	Quantum well second layer
	3	$In_{0.45}Al_{0.55}As$	0.9	undoped	Quantum well third layer
	4	$In_{0.63}Ga_{0.37}As$	2.8	undoped	Quantum well fourth layer
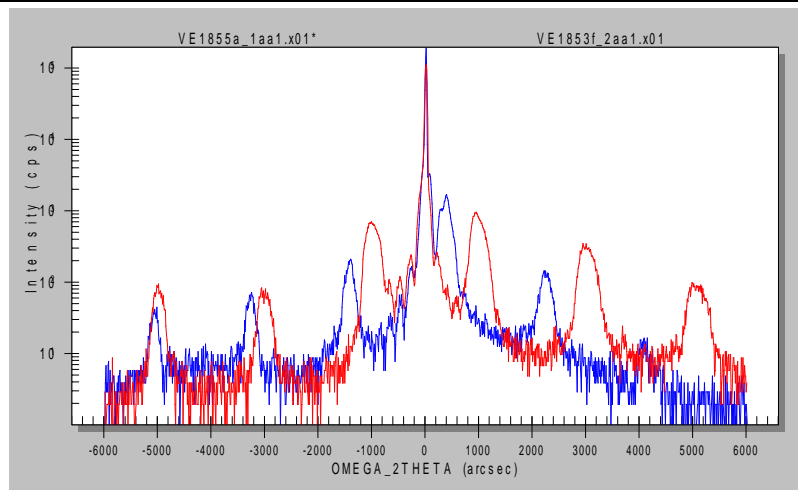
Figure 13. The measured (blue line) and the simulated (red line) X-ray of VE1853.

- According to the X-ray results, we assumed that after the growth the percentage of the As in VE1860 is different from what we designed for that sample. This is due to the competition between Sb and As as group V elements.

Table 3			Sample: VE1871,VE1872		
Layers of a Period	1	InP	1.5	undoped	Quantum well first layer
	2	$GaAs_{0.57}Sb_{0.43}$	1	undoped	Quantum well second layer
	3	$In_{0.45}Al_{0.55}As$	0.9	undoped	Quantum well third layer
	4	$In_{0.63}Ga_{0.37}As$	1.6	undoped	Quantum well fourth layer

- We reduced the thickness of all layers to have a peak at a shorter wavelength as shown in table 3. In VE1872 the As flow was higher for the growth of all layers except for the $GaAs_{0.57}Sb_{0.43}$ layer in comparison to VE1871.

Table 4			Sample: VE1873		
Layers of a Period	1	InP	2.5	undoped	Quantum well first layer
	2	$GaAs_{0.57}Sb_{0.43}$	2.6	undoped	Quantum well second layer
	3	InP	2.5	undoped	Quantum well third layer
	4	$In_{0.63}Ga_{0.37}As$	2	undoped	Quantum well fourth layer

- We removed $In_{0.45}Al_{0.55}As$ in sample VE1873 to see if this layer was responsible for inconsistent results in the previous samples.

Table 5			Samples:VE1875, VE1876 and VE1878		
40X	1	$In_{0.5}Al_{0.5}As$	3.0	undoped	Quantum well first layer
	2	$GaAs_{0.57}Sb_{0.43}$	3.0	undoped	Quantum well second layer
	3	$In_{0.45}Al_{0.55}As$	0.9	undoped	Quantum well third layer
	4	$In_{0.63}Ga_{0.37}As$	3.3	undoped	Quantum well fourth layer

- In VE1876 the Sb flow was decreased as well as the thickness of the InAlAs with regards to VE1875 to match the theoretical and experimental X-ray. In VE1878 the Sb flow has been decreased even more to have a good match (see Figure 14). We removed InP in all of these structures to see if that layer was troublesome in VE1873.

Table 6				VE1886
1	$In_{0.5}Al_{0.5}As$	3.0	undoped	Quantum well first layer
2	$GaAs_{0.57}Sb_{0.43}$	1.6	undoped	Quantum well second layer
3	$In_{0.45}Al_{0.55}As$	0.9	undoped	Quantum well third layer
4	$In_{0.63}Ga_{0.37}As$	2.3	undoped	Quantum well fourth layer

- For VE1886 we reduced the layer thicknesses to see if we could get any PL in the wave.
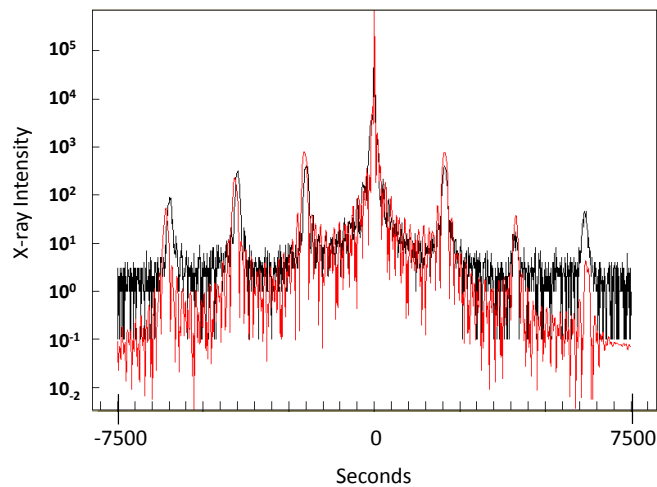
Figure 14. The measured (black line) and the simulated (red line) X-ray of VE1878.

Table 4			Sample: VE1889		
42X	1	$In_{0.45}Al_{0.55}As$	2	undoped	Quantum well first layer
	2	$GaAs_{0.57}Sb_{0.43}$	1.7	undoped	Quantum well second layer
	3	$In_{0.63}Ga_{0.37}As$	1.4	undoped	Quantum well third layer
	4	$In_{0.45}Al_{0.55}As$	0.6	undoped	Quantum well fourth layer
	5	$In_{0.63}Ga_{0.37}As$	1.4	undoped	Quantum well fifth layer
	6	InP	2.5	undoped	Quantum well sixth layer

- In this structure (VE1889) we put the InAlAs layer inside the InGaAs layer to see if the lack of PL in the previous samples were due to the fact that InAlAs was blocking electron and hole type −II recombination when it was between InGaAs and GaAsSb layers. However it turned out that it was not the reason for the lack of PL.

Table 6			Sample: VE1891		
42X	1	$In_{0.45}Al_{0.55}As$	1.5	undoped	Quantum well first layer
	2	$GaAs_{0.57}Sb_{0.43}$	2.0	undoped	Quantum well second layer
	3	$In_{0.63}Ga_{0.37}As$	2.3	undoped	Quantum well third layer

- VE1891 was designed to test the results of Vurgaftman [24]. By removing InP X-ray looked pretty good in comparison to the previous sample.

Table 7			Sample: VE1892		
10X	1	$GaAs_{0.57}Sb_{0.43}$	1.7	undoped	Quantum well first layer
	2	$In_{0.63}Ga_{0.37}As$	1.5	undoped	Quantum well second layer

- VE1892 was designed to have an experimental peak wavelength much shorter than VE1891 in order to see if the lack of PL was due to the fact that the PL peak was beyond the cut off wavelength of the detector.

Table 8			Samples:VE1901 andVE1902		
5X	1	$In_{0.53}Al_{0.47}As$	17	undoped	Quantum well first layer
	2	Q 1.43	18	undoped	Quantum well second layer
	3	$In_{0.53}Al_{0.47}As$	1	undoped	Quantum well third layer
	4	$In_{0.53}Ga_{0.47}As$	3	undoped	Quantum well fourth layer
	5	InP	17	undoped	Quantum well fifth layer

- We then decided to design antimony free quantum wells. Sample VE1902 has the same structure as VE1901 but it was grown on a highly p-doped substrate therefore it contained built in electric field. The X-ray data and simulation of VE1902 has been shown in Figure 15.

- Table 9 summarizes the spectral characteristics of the emitted PL together with the theoretical perditions for all of the introduced samples.
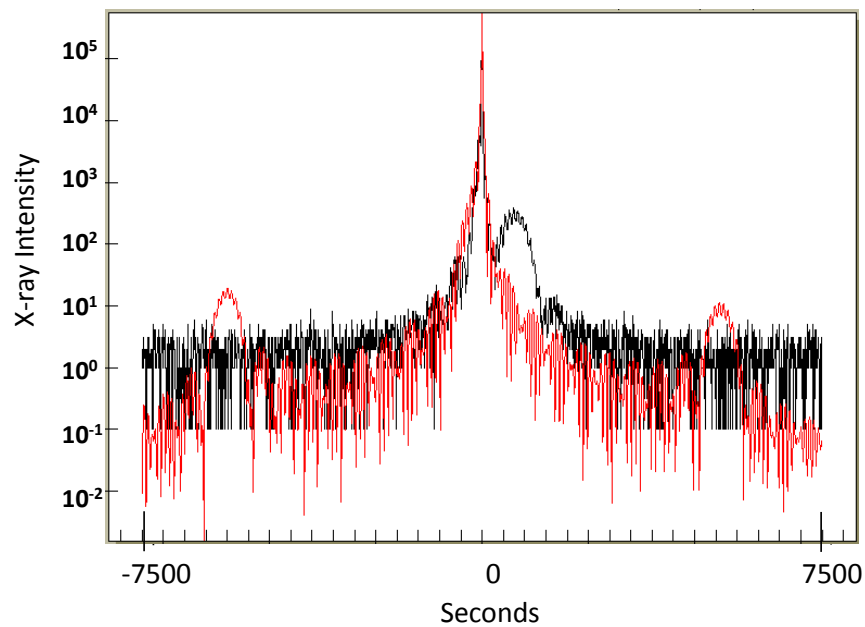
Figure 15 . The measured (black line) and the simulated (red line) X-ray of VE1902.

| Table 9

Sample number	General characteristic of the measured PL	Theoretical value of the blueshift assuming the photo generated carrier density is equal to 10^{18} cm^{-3}	Theoretical PL peak wavelength(nm)	Experimental peak wavelength near center of the wafer	Experimental peak wavelength near edge of the wafer
VE1853	broad	7.6 mev	1632	1652	1487
VE1856	broad	7.6 mev	1632	1513	1644
VE1860	Very broad	3 mev	1325	1657	1484
VE1871	Without PL	0 mev	1280	-------	----------
VE1872	Very broad	0 mev	1280	1655	1518
VE1873	broad	10.3 mev	1612	No peak observed	1518.5
VE1875	narrow	5.64 mev	1631	--------	--------
VE1876	Without PL	5.64 mev	1631	--------	--------
VE1878	Without PL	5.64 mev	1631	--------	--------
VE1886	Without PL	5.64 mev	1631	--------	--------
VE1889	Very broad	2.15 mev	1405	No peak observed	1610
VE1891	Without PL	0.9615 mev	1445	---------	---------
VE1892	Very broad	0 mev	1325	1655	1591
VE1901	narrow	16 mev	1405	1405	1409
VE1902	narrow	16 mev	1405	1405	1409

Thermometry:

- For the detection of optical refrigeration, thermal isolation is important. Therefore the temperature should be measured using methods which ensure good thermal isolation. These methods include non-contact optical measurement, thin film thermistors, thermocouples or any contact thermometry with the use of thermally isolative material such as fiber Bragg gratings.

- There are diverse methods of non-contact optical thermography such as sensitive photothermal deflection technique[25] or more simply by using the florescence spectrum of the material. In this method a spectrum temperature relation can be calibrated over a wide range of temperatures using a thermostat, then the observed spectrum is compared to the reference spectra and the temperature is determined [2].

- Differential luminescence thermometry (DLT) measures the changes in the luminescence spectrum of a solid as a function of temperature. The fundamental band gap energy of most direct semiconductors increases with decreasing temperature. This physical property is a key component of this approach for deducing the temperature change of a material. For more detailed information the reader is referred to the article written by Imangholi et al [26].

- CCD-based Thermo Reflectance Imaging: Thermoreflectance imaging measures the fractional change in the sample's reflectivity ΔR/R in response to surface temperature variations ΔT. The reason why researchers are interested in ΔR/R instead of ΔR is that the drift of the illumination source intensity during the measurement does not generally adversely affect the measurement because the measured thermoreflectance is the ratio of ΔR to R, both of which would change by the same factor. Knowledge of the material wave length and temperature dependent thermoreflectance coefficient (Which is found by calibration) enables the calculation of ΔT from the measured $\Delta R/R$. The setup is shown in Figure 16.. The probe beam from a light-emitting diode
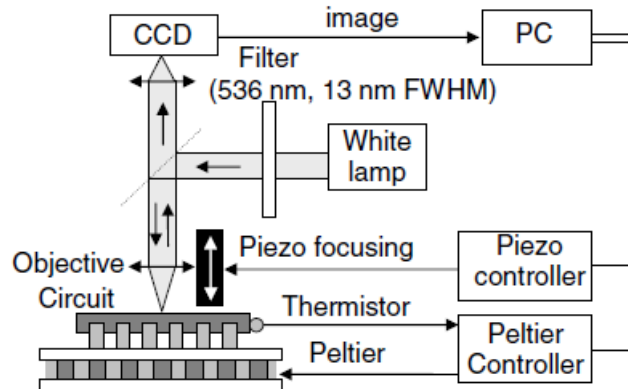
Figure 16. The setup of thermoreflectance CCD imaging[28].

(LED) provides steady illumination on the surface of the test device. Reflected LED light from the surface of the test device is collected through a microscope objective and imaged onto a video graphics CCD array. Because the spatial resolution scales linearly with the wavelength chosen for the measurement, a shorter wavelength can resolve a smaller distance. However, depending on the thermoreflectance spectrum of the material to be imaged (and practical constraints such as the spectral sensitivity of the CCD camera and the availability of a given wavelength for illumination), it may be more profitable to use a slightly longer wavelength.

- Obtaining the thermoreflectance coefficient is a difficult in this method. In general the thermoreflectance coefficient depends upon wavelength, CCD sensitivity, material under test, etc. Therefore a precise calibration is needed for each pixel of the CCD which represents a part of surface. It is very important to conduct a careful spectral sensitivity study of thermoreflectance coefficient in order to optimize the signal to-noise ratio [27]. Two approaches exist to investigate the wavelength dependent reflection coefficient: one, the most straightforward solution uses a monochromatic light source of variable wavelength to illuminate the sample and acquire a thermal image. Two, the sample is illuminated with a thin line-shaped beam of white light. The light reflected from the sample is then spectrally dispersed using a grating on the CCD camera, along a direction perpendicular to the line-shaped beam. Therefore, if a line is isolated on these images along the dispersion direction, a spectrum $R(\lambda)$ or $dR/dT(\lambda)$ is obtained directly[27]. Moreover since the spectral response of silicon-based CCDs is not flat It is necessary to use a reference mirror of known reflectivity on which we obtain a reference spectrum $I_{ref}(\lambda)$. The optical reflectivity is then given by $R(\lambda)=I_{opt}(\lambda).RAl(\lambda)/I_{ref}(\lambda)$.

One of the main experimental difficulties of calibration for thermoreflectance technique is linked to thermal expansion [27]. The vertical movement of the sample causes defocusing and therefore information loss. The position of the optimal focus has to be determined in order to mechanically correct the position of the objective. This is relatively straightforward in an imaging setup: the sharpness of the image is obtained by calculating the average value of a 2D gradient (spatial derivative) over the image, which is a good indicator of the quality of the focusing when sharp details exist in the imaged area. By plotting the value of this parameter for several positions of the objective, a maximum can be extracted, corresponding to the best focus. Under high magnifications, typically above 20×, a lateral displacement caused by inhomogeneous expansion is also observed. This movement causes no information

loss but has to be corrected in order to be able to measure the reflectivity of a chosen region of the sample. This problem can be overcome by calculating the translation that optimizes the correlation of the current image with a reference image.

- The setup for calibration is shown in Figure 17 and is done as follows: (1) Fixing a temperature T and waiting until the thermal equilibrium of the sample is reached. (2) Finding the best focus. (3) Correcting the lateral translations of the image. (4) Measuring the reflectivity $I(T)$ in one or more regions of the image. Since $I(T)/I(T_0) = R(T)/R(T_0) \approx 1 + (1/R(T_0))(\partial R/\partial T)(T - T_0)$, a linear fit to the values of $I(T)/I(T_0)$ gives a slope $1/R(T0)(\partial R/\partial T)$ which is equal to reflection coefficient[27].
  Obviously a Peltier element control of the whole test sample is needed for calibration. Due to the lack of the facilities needed for calibration and realization of this method. We looked for simpler methods of thermometry.
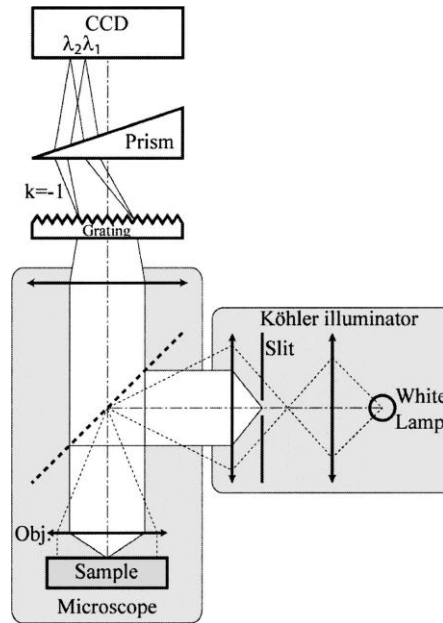
Figure 17. setup for the measurement of the spectra of $R(\lambda)$ or $dR/dT(\lambda)$[28].

- Fiber Bragg Grating (FBG): this method is based on the change of the resonance wavelength of a FBG with temperature. We have used this method to measure the temperature of the samples with fabricated ridges. We developed a Labview program to monitor the changes in the resonance wavelength and to calculate the change of temperature accordingly. This method is simple to use, accurate up to 0.1 degrees and is thermally non-perturbative since silica which the FBG is made from is thermally isolative. However since a contact between the FBG and sample is required this method is inappropriate for thermometry of small and delicate samples.

- Thermocouple thermometry: this is one of the most famous ways of thermometry which is based on Seebeck effect. Usually two different metals with different Seebeck

coefficients are chosen. Two metals should be connected at one end. If the temperature of the junction changes the voltage difference between the other ends of the metals changes l. Due to its simplicity and ease of fabrication, thin film thermocouples have been used extensively. We are also going to use thin film thermocouples using nickel and chromium. We have all the facilities required for fabrication of thin film thermocouples. The estimated sensitivity is 10 µV/C, which is good enough for our purpose. We will use low noise amplifiers to have a higher sensitivity and to increase the signal to noise ratio.

- Thermistor: thermisotor work based on change of resistivity with the change of temperature. Thin film thermistors have been used extensively like thin thermocouples. They can be fabricated with only one lithography followed by metal lift off. We are using nickel both for one of the metals of the thermocouples and also as a thin film thermometer. The thermal coefficient of of a 50 nm thin film nickel is 3700 ppm/k according to [29]. In Ref [29] a complete study of nickel as a thin film thermoresistive sensor is presented.

- Both thermocouple and thermistor are used in our final device for the purpose of comparison and calibration

Experimental setup

Experimental setup:

- Dynamic measurement of the output beam of the modulator needs a very stable setup. It should have the capability of accurate illuminating of the modulator and collecting the output beam.

- Manual positioning instruments include two xyz stages, tilting, rotating and the necessary mount stages. One of the xyz stages is used for these alignments and adjustment of the laser beam with the facet of the ridge waveguide. The other one is used for collecting the output beam of the modulator.

- Lenses and collimators are needed for focusing the input beam into the ridge waveguide. They should be also used for collecting the divergent output beam going out of the waveguide.

- Microscope: for seeing the chip and for connecting the probes to the modulator's leads. Our microscope consists of two parts: infrared and optical part. The optical part

consists of a visible camera and a blue (450 nm) LED for thermoreflectance measurements. A Matlab software was developed to concurrently get data from the visible camera and show the convergence of the Lock-in thermoreflectance signal in real time.

- Laser source. We use two laser sources. One of them is a continuous wave laser near 1.55 μm and the other one is a pulsed laser which is able to produce pulses with widths as narrow as 300 fs.

- Spectrum analyzer. It is used for recording the spectrum of a beam in our measurements

- High speed optical and electrical oscilloscope.

- Fibers: Both single mode polarization maintaining lensed fibers and the conventional fibers are required. The first is used in our future experiments in order to remove the lenses and the collimator so that we will have more space to do the experimental investigations. The conventional fibers are used to deliver the laser beam into the

(a)   **(b)**
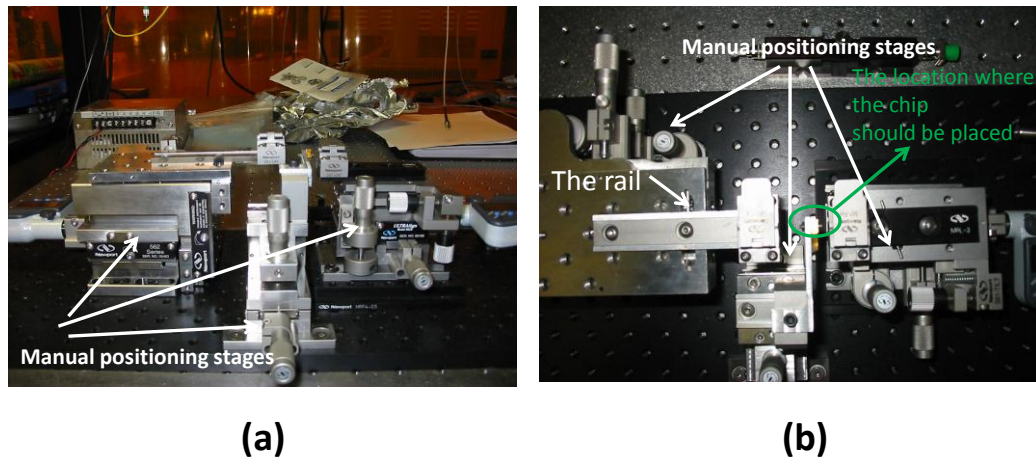
Figure 18. The measurement setup (a) Side view (b) Top view.
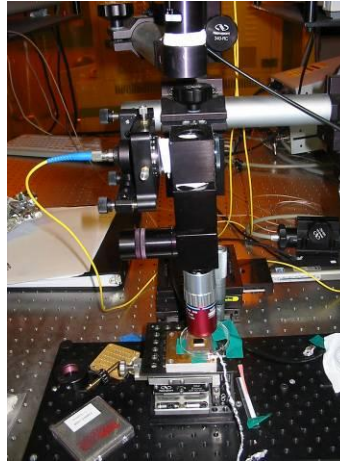
Figure 19. the Microscope.

Measurements:

- Using the prepared setup a dc voltage was applied to a conventional modulator and the transmission of a continuous wave laser was studied by sweeping the laser wavelength. The result is shown in Figure 20.

- The main low frequency sinusoidal behavior of the transmission versus the laser wavelength is due to the Fabry-Perot oscillation in the modulator as a cavity.

- We believe that the faster oscillation of the transmission which is evident for lower output power in the logarithmic plot is because of the Fabry-Perot oscillations in a bigger cavity formed by two input and output lenses.

Wavelength sweep near 1.55 um at the DC voltage of -5 V
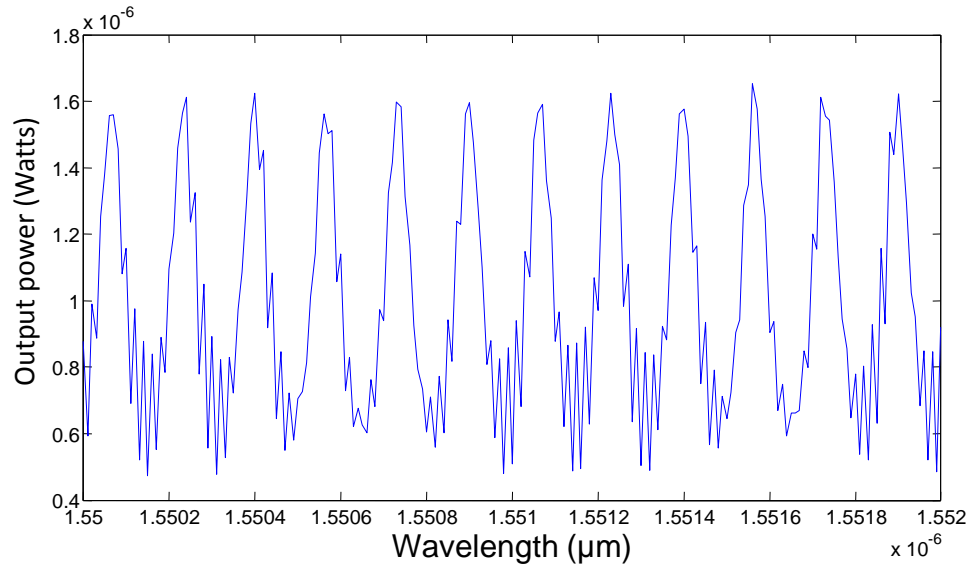
Figure 20. Fabry-Perot oscillation shift in a 2 mm long phase modulator when the applied bias is -5 volts.

- We fabricated ridges on the MQWs structure as explained in the processing section. Then we focused both CW and pulse laser to measure and test different quantities of interest.
- In the first experiment, only the CW laser was used. First the wavelength was scanned in order to obtain the transmission versus wavelength as shown in Figure 21.
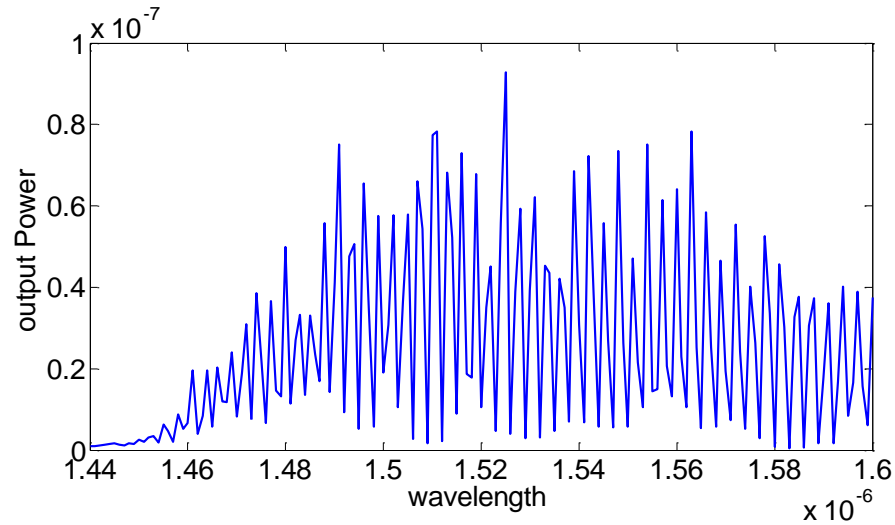 It is clear from Figure 21 that:
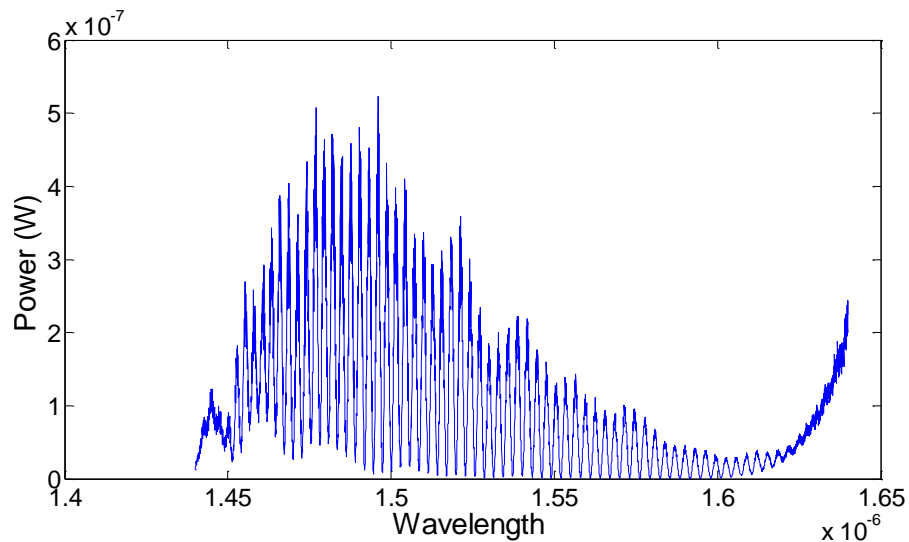
Figure 21 . Output power when the device is scanned with a 900 µW CW laser in the wavelength range as shown the resolution of this scan is 1 nm and the averaging time of the detector was set to 0.1 seconds. The length of the devices is 1 mm.

1-The period of the oscillations doesn't change over the entire spectrum and is close to 3 nm.

2-The oscillations start at 1444 nm and ends gradually near 1625.

3-By comparing the results with those of a 2 mm device as shown in Figure 22 we see that the period of the oscillations is the same which rules out the optical interference as a mechanism of producing output power oscillations. On the other hand the period in the wavelength is 3 nm which corresponds to a cavity of 0.114 mm. we couldn't think of this cavity to be anywhere within the measurement system.

4- The steep slope of the output power for wavelengths longer than 1.6 um indicates a considerable absorption. According to the simulations and the PL spectra, the absorption should be negligible in that wavelength range. Furthermore by changing the polarization using the polarization controller the absorption changes which means that this absorption is coming from a quantum well. The only layer which is responsible for this absorption is the bottom InGaAs layer which is the layer number 2 in table 10. The absorption of the light by this layer leads to heat which is not desired. Therefore we came with new ideas such as backside etching and fabrication of suspended waveguides to remove this absorbing layer.

Table 10. the final grown sample (VE1946) together with refractive indices of its layers at 1.55 μm.

Layer #	Material	Thickness (nm)	Doping	Refractive index@1500nm
1	InP		n-doped	Refractive index(1550nm)=3.17 using the index calculator Alpha=1 cm^{-1}
2	In$_{0.53}$Ga$_{0.47}$As	100	N=10^{18} cm^{-3}	Refractive index using the index calculator=3.69 Alpha=7e3 cm^{-1}
3	InP	1000	Ramped N=10^{18} cm^{-3} to N=10^{17}	Refractive index3.17 using the index calculator Alpha=0.32 cm^{-1}

4		InP	500	$N=10^{17}$ cm^{-3}	Refractive index=3.17 using the index calculator Alpha=0.12
5X	1	In$_{0.53}$Al$_{0.47}$As	17	Undoped	A constant refractive index for active region according to the cut off wavelength of the PL=1.48 um as a value for bandgap of the quaternary and the index calculator = 3.51 Alpha=2e4 cm^{-1} (an approximate value)
	2	Q 1.43	18	Undoped	
	3	In$_{0.53}$Al$_{0.47}$As	1	Undoped	
	4	In$_{0.53}$Ga$_{0.47}$As	3	Undoped	
	5	InP	17	Undoped	
6		InP	500	$P=10^{17}$ cm^{-3}	Refractive index(1550nm)=3.17 using the index calculator Alpha=1 cm^{-1} (approximate value)
7		Q 1.2	15	$P=10^{17}$cm^{-3}	The band gap was first calculated by the matlab program with the presense of buit in electric field=1.46 and the refractive index was calculated according to the index calculator=3.09 Alpha=0
8		InP	1000	$P=10^{17}$ cm^{-3} Ramped up to $P=10^{18}$	Refractive index 3.17 using the index calculator The absorption

				coefficient=20 cm-1
9	$In_{0.53}Ga_{0.47}As$	50	$P=2x10^{18}cm^{-3}$	The same as the second layer

Figure 22. Output power when the device is scanned with a 900 µW CW laser in the wavelength range as shown the resolution of this scan is 1 nm and the averaging time of the detector was set to 0.1 seconds. The length of the devices is 2 mm.

- We first suspected that maybe these oscillations are coming from the deficiency in our laser. Therefore we checked the spectrum of both pulsed and CW lasers using the optical spectrum analyzer. We used attenuators at the output of the lasers in order to protect the optical spectrum analyzer. The spectra don't have any periodic feature which shows that the lasers work in good condition. The results are shown in Figure 23 and Figure 24.

- Since for the purpose of cooling, we need to use pulsed laser near 1550 nm in order to have a dynamic stark effect within the quantum well, we have done a wavelength scan near 1550 nm with the highest resolution possible as shown in Figure 25. It is evident that the period of the spectrum doesn't change when the different powers of laser have been used but a shift of the spectrum is clearly observed in this case. The shift of the spectrum is attributed to the change of dielectric constant of the material
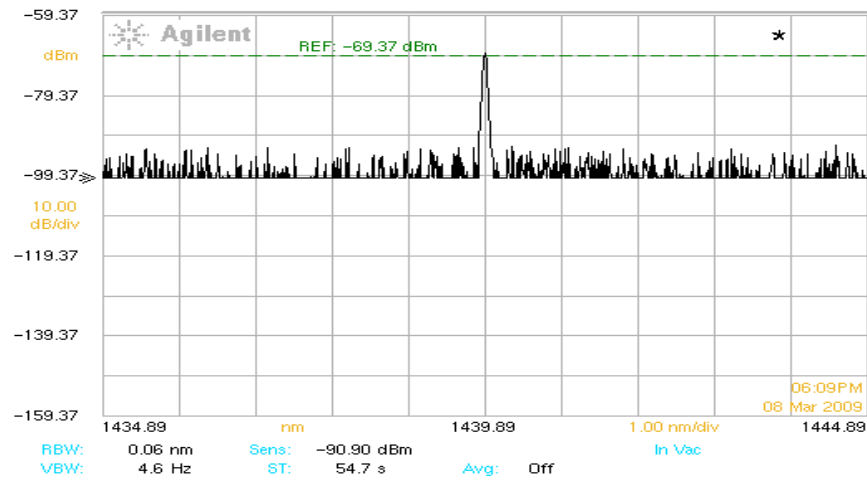
Figure 23. Output spectrum of the CW laser.
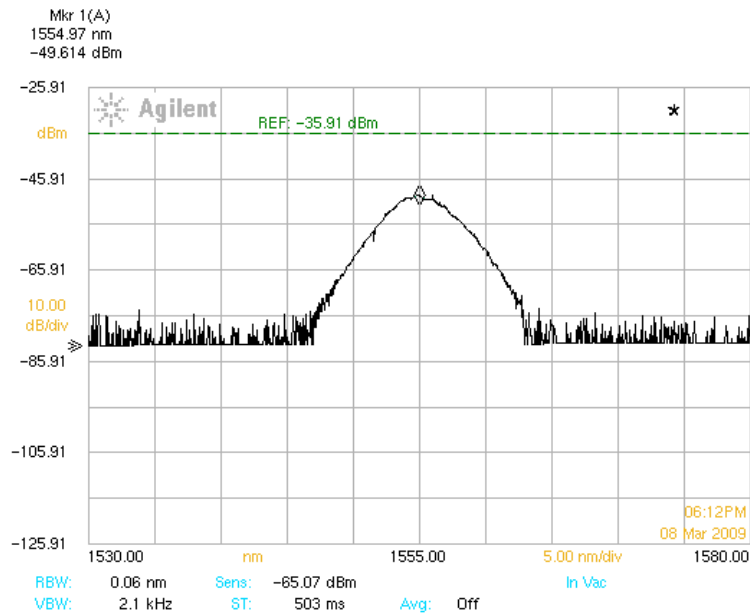
Figure 24. the spectrum of the input pulse beam.

caused by laser absorption and the change of temperature. In Figure 26 the spectra of the TM mode has also been shown. We still see a periodic change of power for TM mode but with a much lower relative magnitude. Similar results were also obtained for 4 um and 5 um ridges.

- The wavelength of the minima of the TM spectrum is very close those of 100 uW TE spectrum according to Figure 26 which supports the fact that the periodic oscillations of the output power arises because the beam is not purely TM and a small fraction of the signal's power is TE.
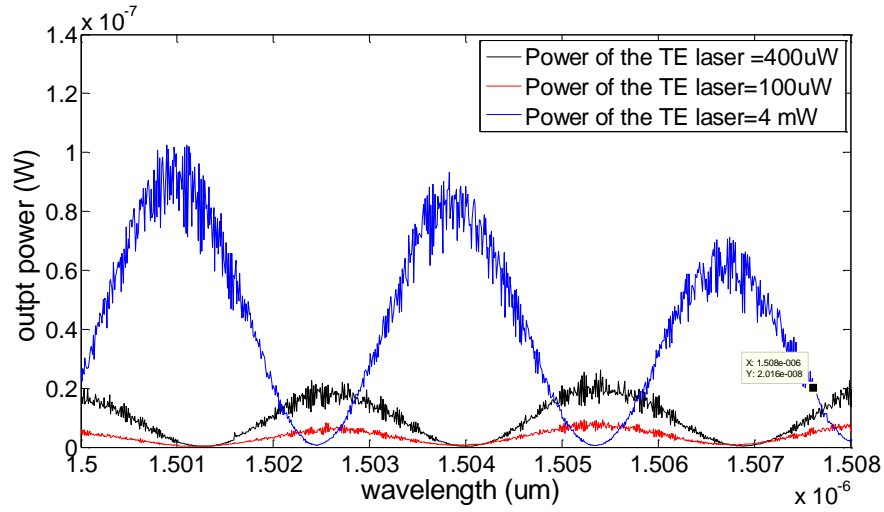
Figure 25. Output power versus wavelength for different input powers for TE polarized laser as indicated in the inset. It is evident that by increasing the input power the spectrum is shifted toward higher wavelengths but its period does not change.
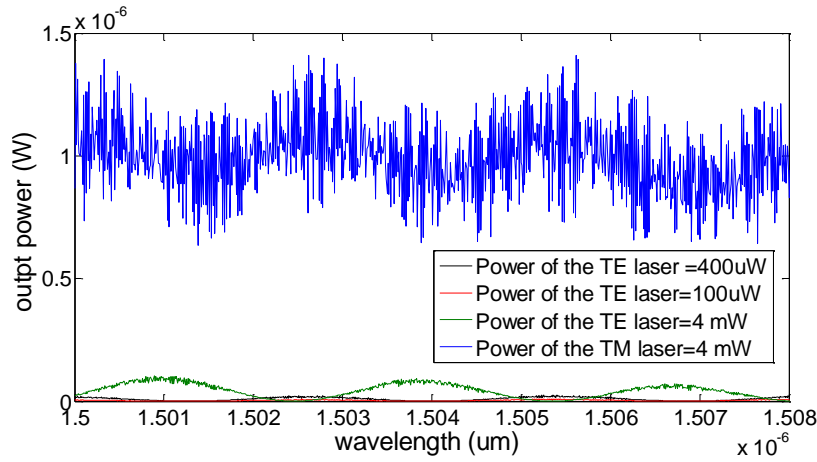
Figure 26. Output power versus wavelength for different input powers, TM polarized light is also included for comparison.

- In order to have a better understanding of the periodicity of the output power versus wavelength, the backreflected power versus wavelength was measured and is shown in Figure 27. The amplitude of this backreflected power is not changing significantly as in Figure 25 and also the period is not 3 nm it is 0.17 nm which corresponds to a cavity length of 2 mm as expected. The change of the power for the backreflected light is 30%. Similar results were also obtained for 4 um and 5 um ridges.
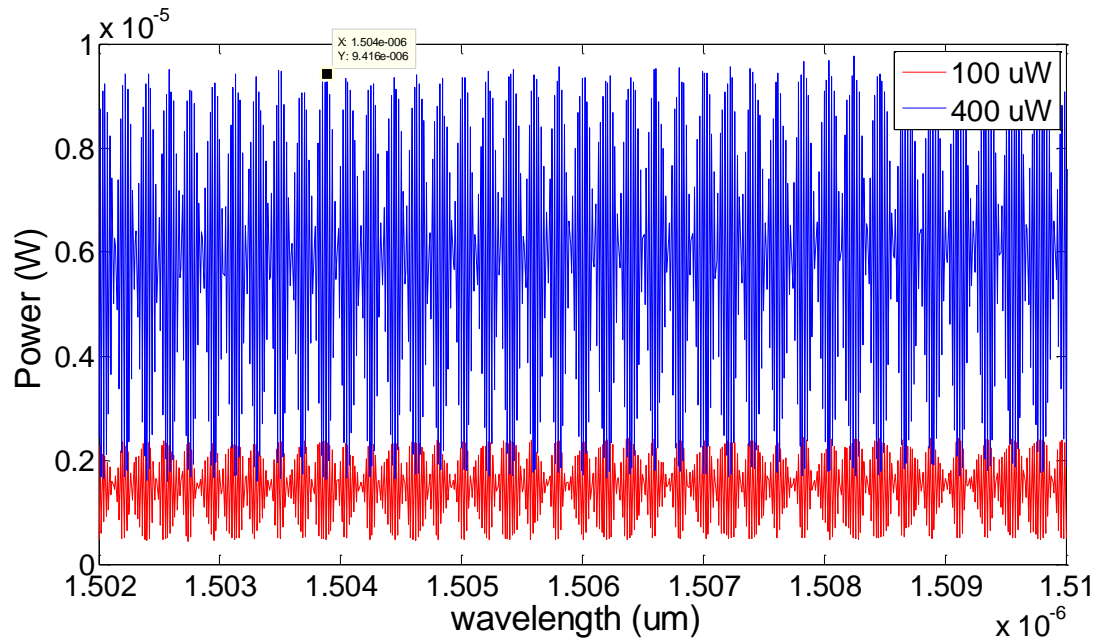
Figure 27. The spectra of the backreflected light obtained by sweeping a TE CE lasers for different powers as indicated.

- According to Figure 28 the maximum change of the backreflected power occurs for TM mode which doesn't get absorbed within the device. For a TM mode we can write:
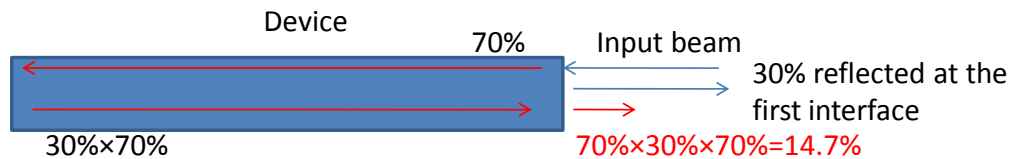
Figure 28. A schematic showing the reflections of the device.

- Next a full scan for obtaining the spectrum of the polarization controller's transfer function has been performed (see Figure 29). Obviously there are some oscillations in its spectrum in the range of 1450 nm to 1550 nm with a maximum extinction ratio of 0.4 dB while the increase of power over the whole spectrum is 0.9 dB. The period of these oscillations is near to 3 nm. This suggests that these oscillations might have led to the oscillations with high extinction ratio in the device output. It should be noted

that if the polarization changes by this period then the extinction ratio in the output of the device gets amplified since the device absorbs TE mode much more than the TM mode.
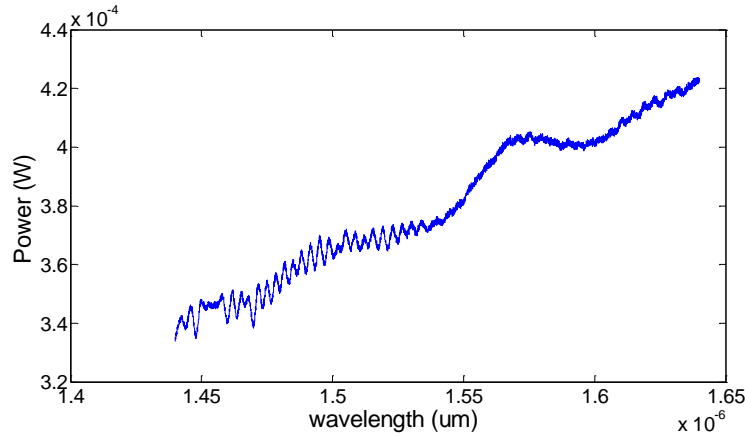
Figure 29. the spectrum of the polarization controller for the TE polarized light.

Profile of the laser beam along the ridge:

- We have also measured the intensity profile of the laser along the ridge using our sensitive infrared camera which is hooked on the optical microscope. A beam splitter is used in the microscope to provide the beams for both visible and the infrared cameras. The infrared camera is sensitive even for beam powers in Pico watts regime around 1.55 um.

- The line profile for the 5 um ridge versus power has been shown in Figure 30. The periodic behavior of the intensity is evident after a certain distance from the facet. The anomalous behavior of the intensity near the facet might be caused by the mixture of the beam that has not been focused into the ridge with the coupled beam. The averages in the inset of the figure show a slight decrease of the period with decreasing the input power.

- Figure 31 shows the measurement results of the line profile for the 4 um ridge. Figure 32 also includes the results when the TM beam was coupled into the ridge waveguide.
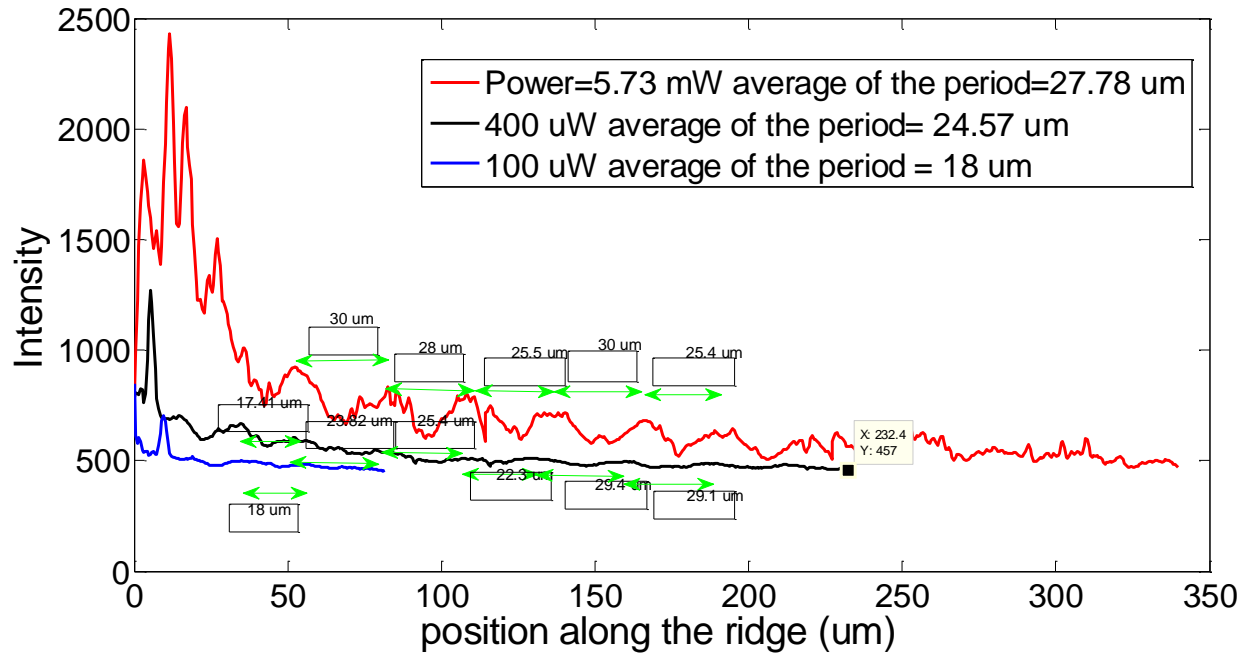
Figure 30. line profile of the CW TE laser with the wavelength of 1500 nm for different powers along the 5 um ridge. The average of the period for each case has been also calculated.

- The line profile of the 3 um ridge has been shown in Figure 33. In this case the periodic shape of the line profile is not resolvable. This might be due to the fact that the 3 um ridge can only support one optical mode.
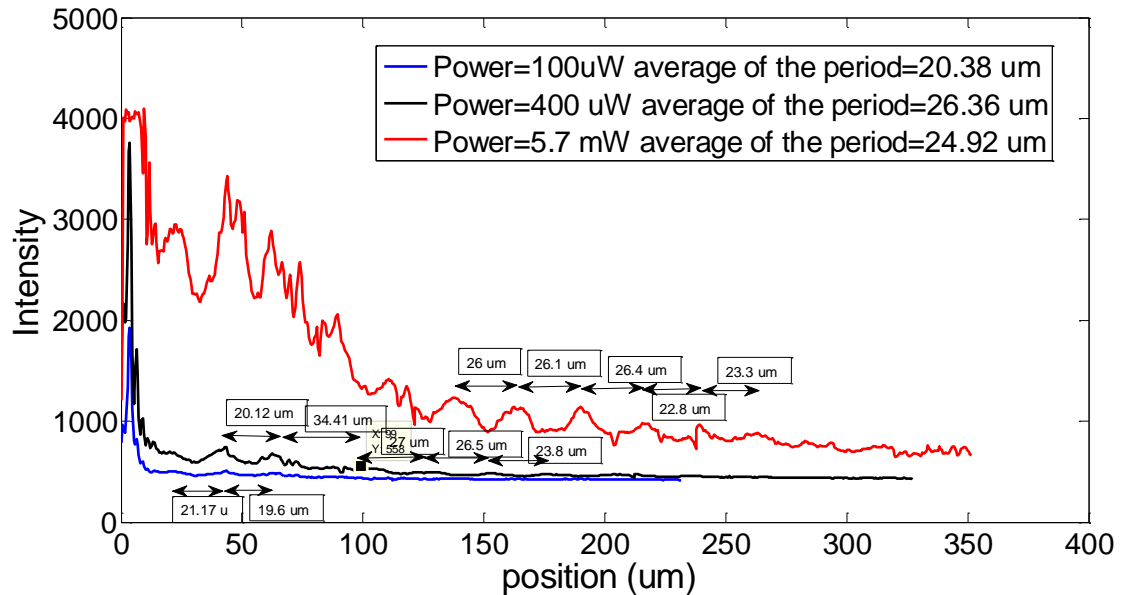
- **Figure 31. line profile of the CW TE laser with the wavelength of 1500 nm for different powers along the 4 um ridge. The average of the period for each case has been also calculated.**
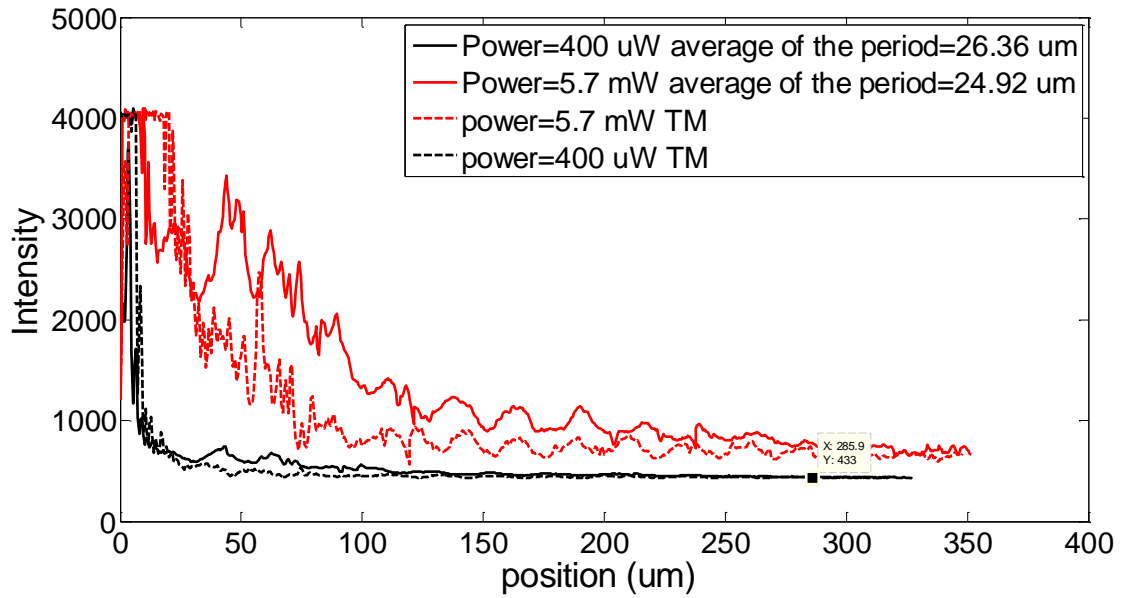
Figure 32. line profile of both TE and TM modes for the 4 um ridge. The wavelength of the laser is 1500 nm.
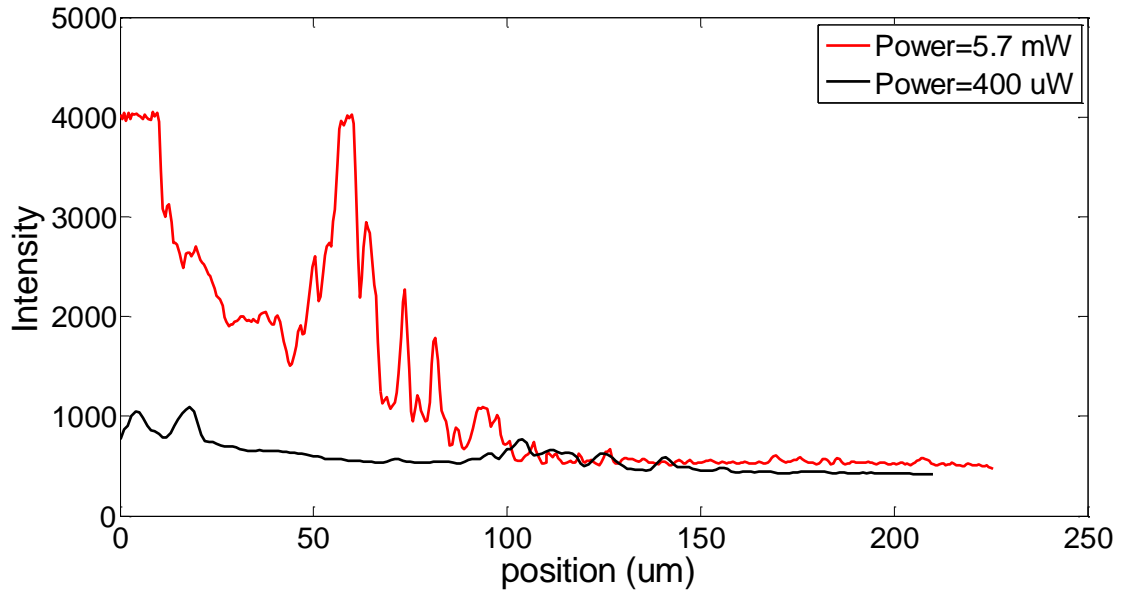
Figure 33. the line profile of the 3 um ridge for the TE laser that has a wavelength of 1500 nm.

THz Radiation

- We also suspected that the periodic response of the device is coming from THz radiation because according to [30] asymmetric quantum structures which are excited below bandgap can emit THz waves. In these devices the pump beam populates two quantum levels partially. Then the quantum coherent oscillation between the two

levels leads to charge motion within the device because the wavefunctions are spatially separated. The motion of charges generates THz waves.

- We executed the Matlab script which was previously used to design the MQW in order to find the energy level differences. The results are summarized in table 11.

- The result of pump probe measurement in which a TE polarized CW laser is used as the pump and a TM polarized CW laser is used as the probe is shown in Figure 34. From this figure it is evident that the changes of the power of the TE laser don't affect the transmission of the probe which indicates that the response of the system is not nonlinear and is not affected by THz radiation.

Table 11

Carrier density	The difference between the topmost heavy hole levels	The difference between the first heavy hole and the first light hole level
$5*10^{17}$ cm-^{3}	34 mev	43 mev
10^{18} cm-^{3}	26 mev	38 mev

- If we want to attribute the 3 nm period at 1440 nm to an energy difference between the levels we calculate the corresponding cavity length to be:
  $L=\lambda^2/(2n\Delta\lambda)$= 104 um
  Which is equivalent to energy of 11.9 meV and is not close any of the values listed in Table 11. Also this cavity length is very different from the periodic spatial line profile which is approximately 25 um, ruling out any relation between the line profile periods and the wavelength period of output power spectrum.

- We also couldn't find any published article which shows that Thz can make the output spectrum periodic as in our case. Therefore we proceeded to find other reasons for justification of oscillations of the output spectrum.
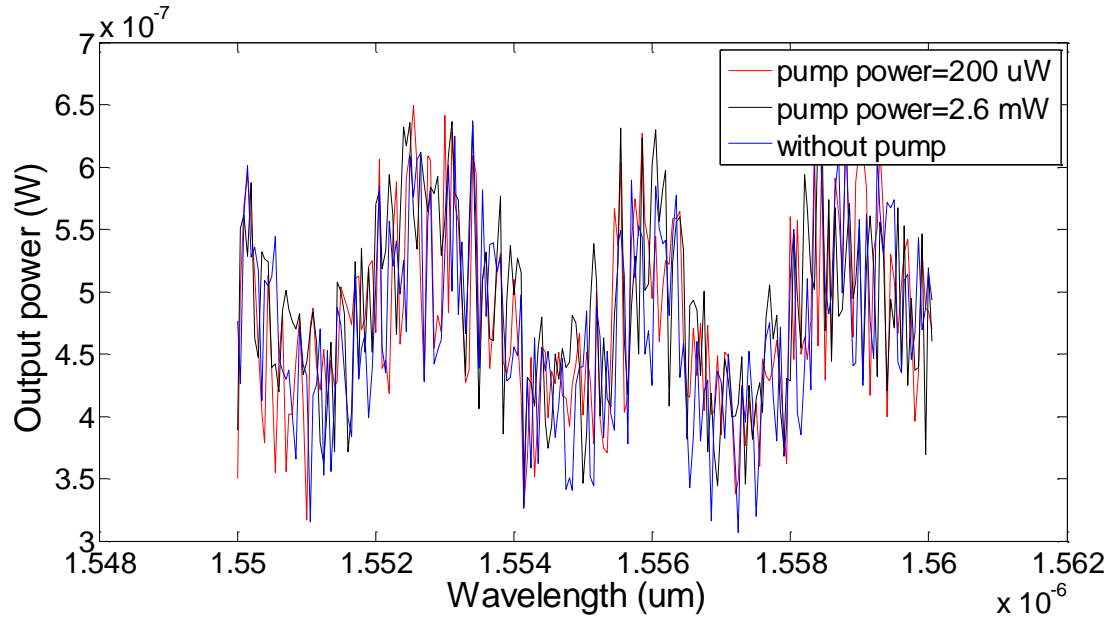
Figure 34. pump probe measurement for the 3 um ridge. The pump r was a TE polarized laserat the wavelength of 1470 nm and the probe was a TM polarized laser with the power of 4mW.

Comparison of the results for different ridges

- In this section the results for different ridges are compared. It is evident from Figure 35 and Figure 36 that as the ridge width decreases the spectrum shifts toward right.
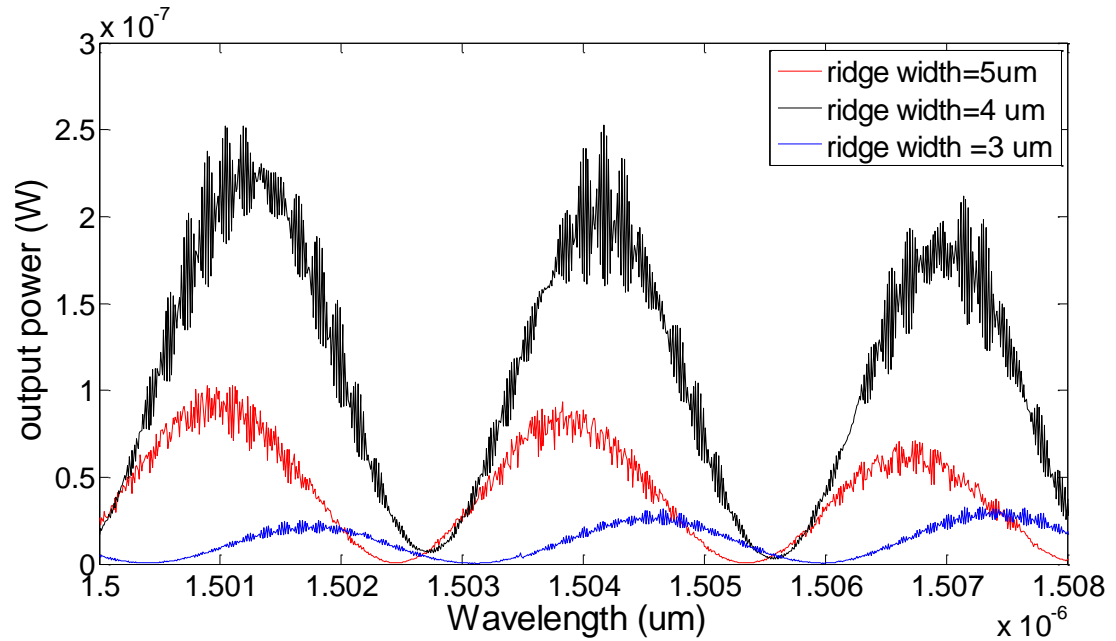

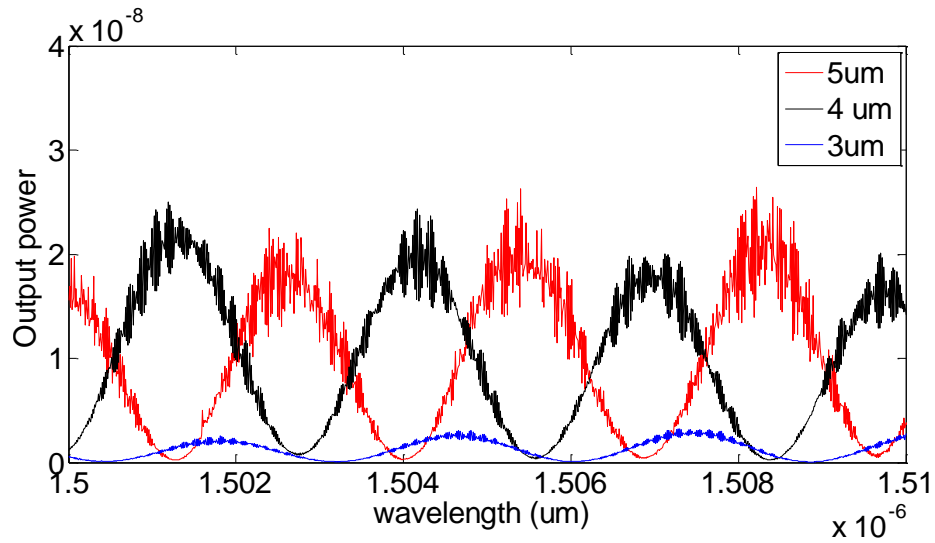**Figure 35. the frequency response of different ridges for a TE excitation of 4 mW.**

Figure 36. the frequency response of different ridges for a TE excitation of 400 uW.
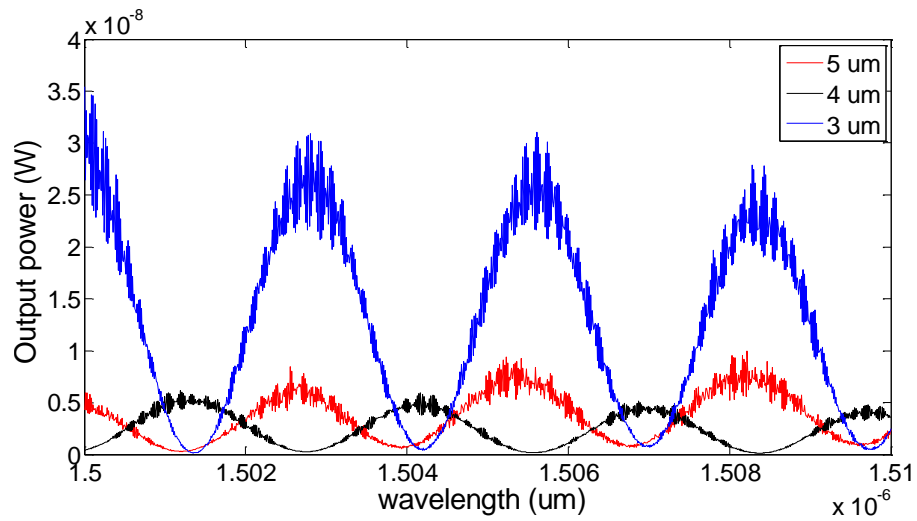
Figure 37. the frequency response of different ridges for a TE excitation of 100 uW.
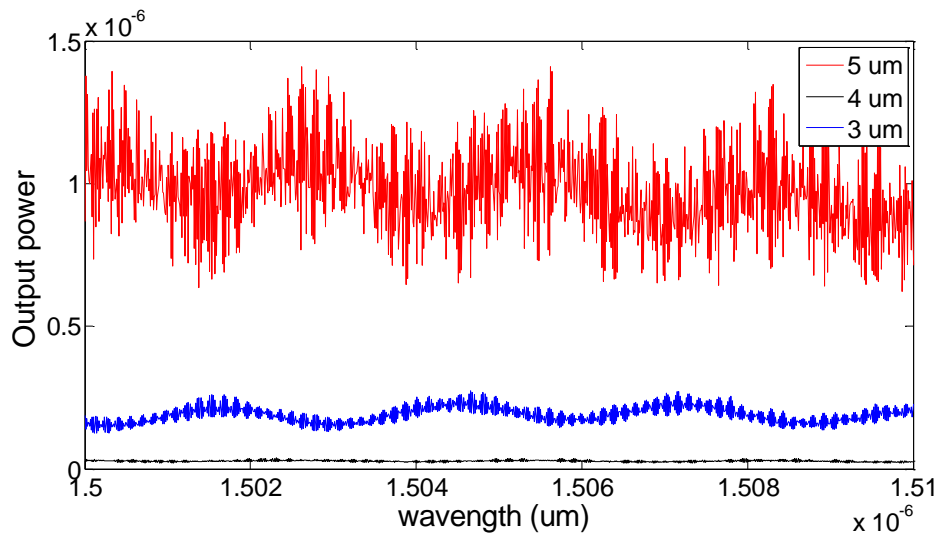
- **Figure 38. frequency response of different ridges for a TM excitation of 4mW.**
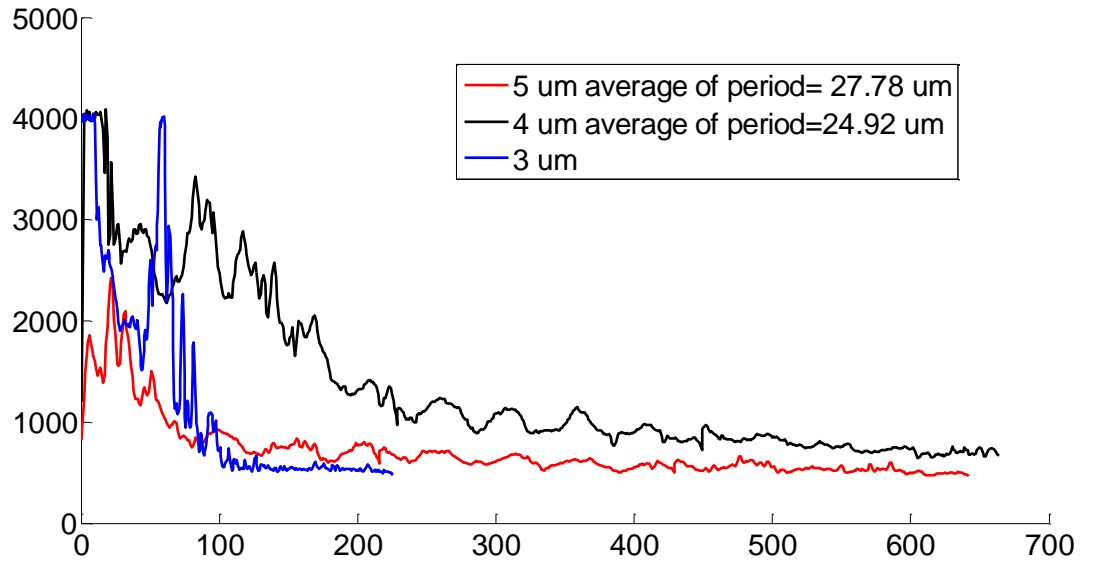
Figure 39. the line profile for different ridges when the laser is TE polarized and its wavelengths is 1500 nm. The power of the laser is 5.7 mW. The average of the periods is also shown.

- The spectra of the TM mode for different ridges are also shown in Figure 38.

- Figure 39 shows that the period increases when the ridge width increases and the density of the photogenerated carriers decreases. Similar trend has been shown for each of the 4 um ridges decreases the density of photogenerted carrier decreases and the period increases. Since the reverse is true for the 5 um ridge, no conclusion can be made at this time.

Calculations based on the obtained results:

- First the spatial periodicity of the line profile is used:

$$\frac{2\pi n_1}{\lambda} P - \frac{2\pi n_2}{\lambda} P = 2\pi \tag{1}$$

In the above equation P denotes the spatial period which is approximately 25 um. λ is the wavelength and it is equal to 1.5 um. Hence n_1-n_2 equals to λ/P which is 0.06. This is a reasonable value corresponding to the refractive index difference of two different optical modes coupled into the waveguide.

- Second by using the periodicity of the spectrum:
  If L is the length of the device then we have the following relation:

$$\frac{2\pi n_1}{\lambda_m}L - \frac{2\pi n_2}{\lambda_m}L = 2\pi m \tag{2}$$

In which λ_m is the wavelength of the m*th* maximum of the spectrum.
Therefore we have:

$$\lambda_m = \frac{L(n_1 - n_2)}{m} \tag{3}$$

Now we want to find the period of the spectrum therefore we take the derivative of the λ_m with respect to m and set Δm equal to one:

$$\Delta\lambda_m = \frac{L(n_1 - n_2)}{m^2} \tag{4}$$

Now if we find m from Eq.3 and put it in equation (4) we finally arrive at the following equation for $\Delta\lambda_m$:

$$\Delta\lambda_m = \frac{\lambda_m^2}{L(n_1 - n_2)} \tag{5}$$

Or equivalently:

$$(n_1 - n_2) = \frac{\lambda_m^2}{L\Delta\lambda_m} \tag{6}$$

Now we know that $\Delta\lambda_m$=3e-9 m L=2e-3 m and λ_m=1500e-9 m therefore Δn= 0.375 which is very different from the result obtained by spatial periodicity of the lineprofile. Therefore these two phenomena are *not related.*

- In order to confirm the conclusion that polarization of laser changes slightly with wavelength, we checked the fibers. Both types of fibers (PC-PC and PC-APC) fibers were used for this experiment. The output of the fiber which is connected to the laser shine light to a prism which separates the s-polarized and p-polarized light into separate orthogonal directions. The results of this experiment showed that a little change of the polarization within the fibers by the change of wavelength is in fact responsible for the anomalous results we obtained. Therefore doing the experiments with polarization maintaining fibers is strongly recommended.

Temperature measurement of the system using fiber Bragg gratings:

- We have used fiber grating in order to measure the temperature of the sample after laser illumination. We put the fiber orthogonal to the ridges on top of the sample. A thin layer of UV epoxy glue was used to attach the fiber to the sample. The sample was hanging in air using the fiber and the fiber itself was horizontally oriented and fixed at two points.

- We noticed that over time the fiber rotates, fortunately we found out that the problem of rotation can be solved by using two rubber pieces which hold fiber more tightly at the anchor points. After that there is no significant vibration and rotation and the system is suitable for temperature measurement without misalignment of the laser beam over time.

- Before doing the experiment we did some calculations for estimation of the thermal response of the system. We did a literature review for finding the thermal parameters of the materials and the elements of the measurement system. It showed that the thermal response has an overshoot with a rise time of 0.1 seconds. Fortunately FBG thermometer w fast enough to follow the temperature variation.

- A Labview program was devised in order to monitor the temperature in real time. The result of the temperature measurement is shown in Figure 40. The increase of the
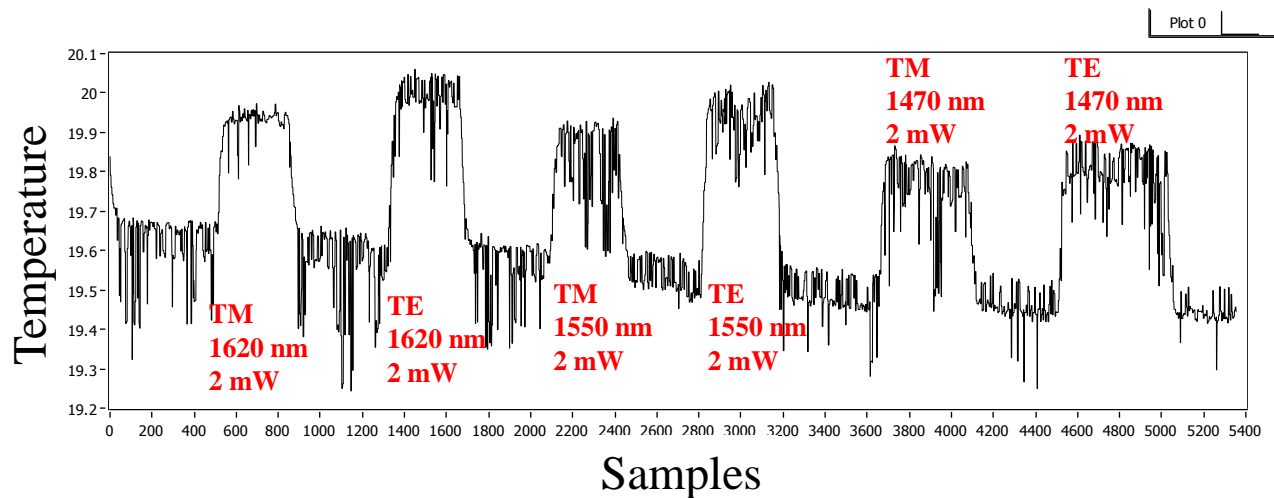
Figure 40. **Temperature of the device after the laser beam is focused into one of the 5 μm ridge waveguides. The horizontal axis shows the sample (data point) number which is used by the labview program to obtain the temperature. As time goes on, the sample number increases. These figure shows that both TE and TM polarizations get absorbed and lead to the increase of the temperature. The polarization, power and wavelength of illuminations have been also specified.**

- The Labview program for the temperature measurement was thoroughly investigated. In this regard real time discrete low pass filtering was implemented. In order to increase the sampling rate the lab view program should be efficient. Therefore it is mandatory to avoid unnecessary calculations. For this reason the program was optimized.
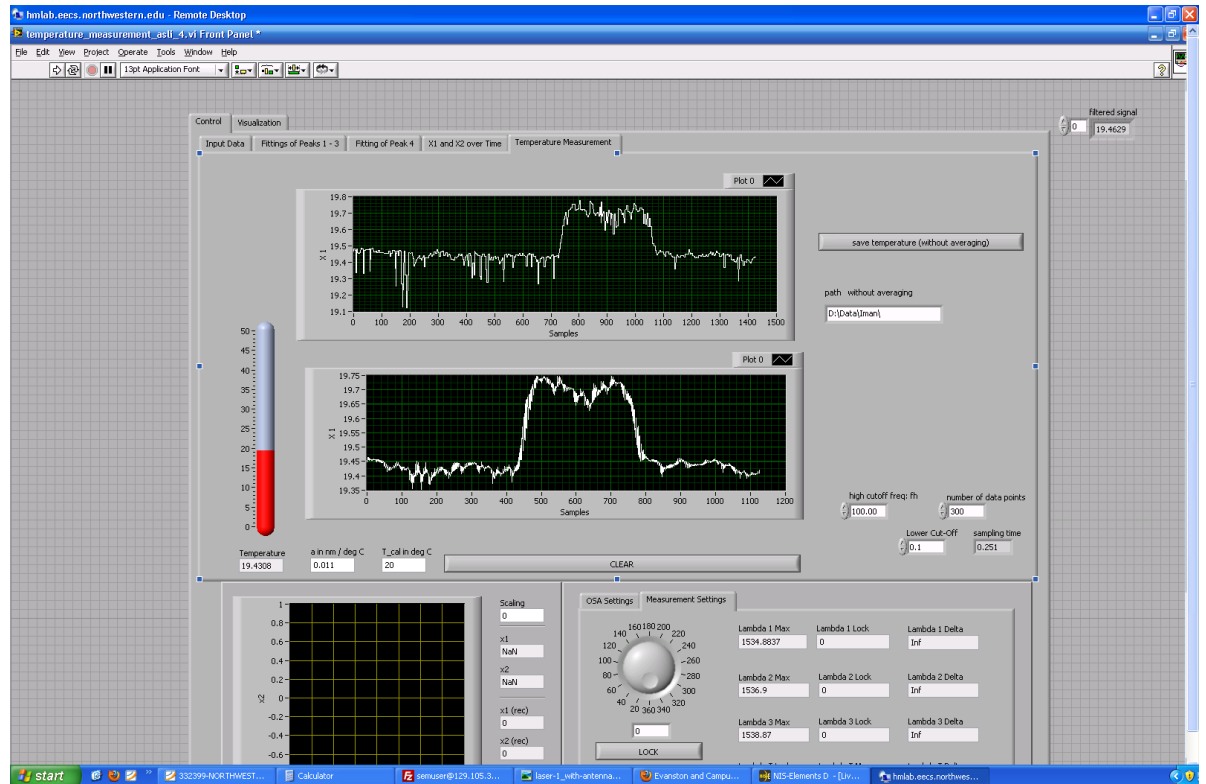

Figure 41. the snap shot of the modified lab view program

- One of the strategies to decrease the computation time and hence increase the sampling rate is to limit the number of data points which go through the filtering process. In this regard the user can define the number of the last data points of temperature for filtering. Furthermore the cut off frequency of the filter is also adjustable. Figure 41 shows the front panel of the program. Both the original data and the filtered one can be monitored during the process. The next attempt is to prepare the program for lock-in purposes for increasing the sensitivity of the temperature measurement. The save option was also included in the program for both the original temperature data and the filtered temperature data so that the user can access and process the measurement results by the generated text files using MATLAB.

Fabrication:

- For the processing of grown MQW structures, we pursued three goals in order to have the best structures for the purpose of laser cooling:
  1. Making good ridge waveguides without any wiggling.
  2. Removing the InGaAs absorbing layer as pointed out in the conclusions of our measurements.

  2- To have a good thermal isolation of the MQW active region with the environment and to make the cooling region as small as possible in order to have a low thermal mass at the end. This strategy helps to increase the thermal sensitivity of the system so that even ultralow cooling powers will produce a large temperature drop which is suitable for thermometry.

- Using standard photolithography the ridges were fabricated as shown in Figure 42. Sample VE1946 was used for processing which had the same structure as VE1902 but with a better quality and more intense PL. The full layer structure of this sample has been summarized in table 10. This table also includes the refractive index calculated with our index calculator program and the values found in the literature.
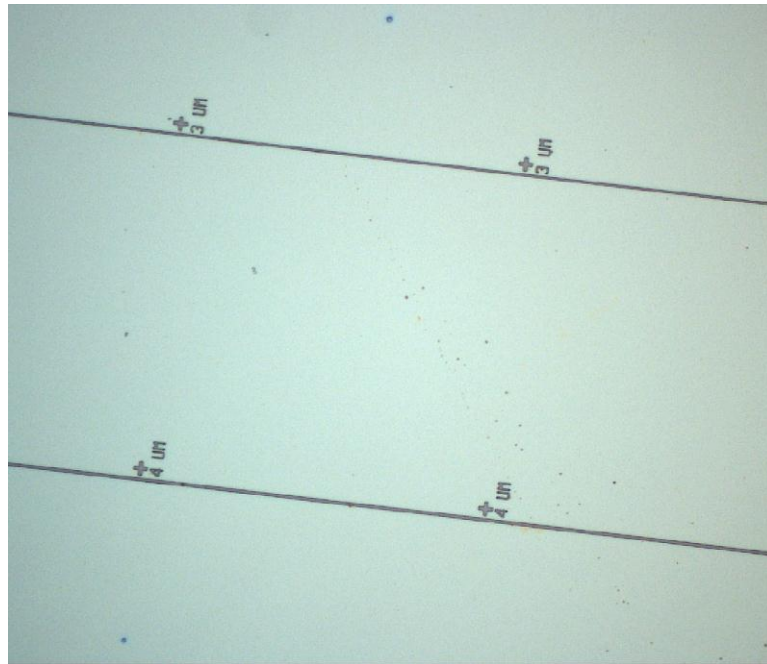

Figure 42. Photo of the fabricated ridge waveguides.

- The process flowchart is shown in Figure 43. First a silicon dioxide layer with the thickness of 100 nm was deposited using PECVD. Then the photoresist was patterned to form the 3, 4 and 5 μm ridges. The silicon dioxide layer was etched using buffered HF. Following that the etching of the InGaAs and the upper InP cladding layer was done. All of the fabrication steps were calibrated to give the best results.

- Later, we found out that the wet etching of silicon oxides leads to some wiggling along the ridges. These wiggling cause reflection of the beam and are not desirable. Therefore we modified the process and did the dry etching of silicon oxide instead of wet etching. We also proceeded to do dry etching to pass the top most InGaAs layer so that the rest of the etching can be done using the wet etchants for InP. The results were quite promising and the wiggling reduced significantly.

- It should be noted that the samples were lapped and polished from the backside to decrease the thermal mass and increase the temperature measurement sensitivity. The results of temperature measurement of this sample have been presented in the previous section.
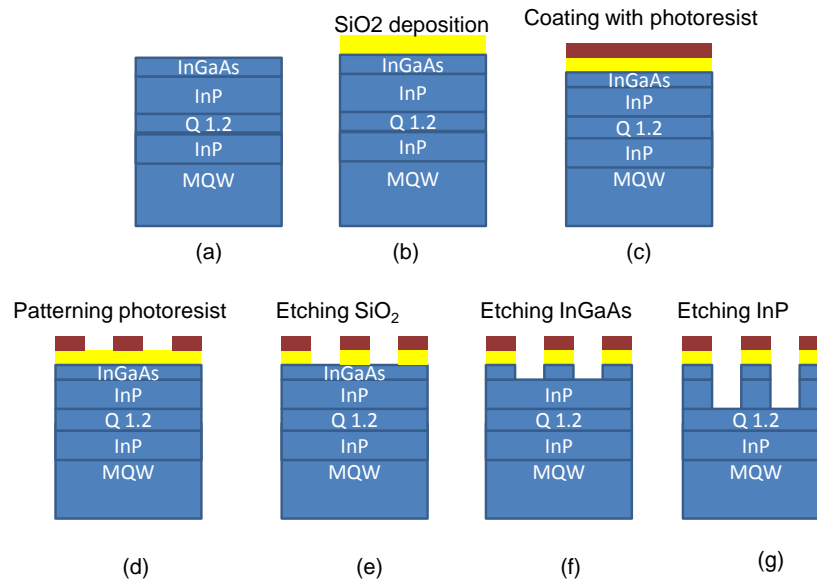

Figure 43. process flowchart for making ridge waveguides.

- In order to remove the bottom InGaAs absorbing layer, the first and most simple idea was to do the backside etching in order to remove the substrate completely and reach the bottom InGaAs absorbing layer. Then we could selectively etch the InGaAs absorbing layer and end up with a very thin membrane of only MQWs and the InP cladding layers. The process flow was as follows:

  I- We did the photolithography and all the processing steps to define the ridge on the sample
  II- We polished the sample and cleave it into small pieces.
  III- We put all the small pieces on a very thin glass-slide bar. The main reason behind using the glass-slide is that it is transparent so that eventually it doesn't block the microscope for seeing the ridges from the top however it is not thermally conductive and can reduce the sensitivity of the temperature measurement to some extent since it is located between the FBG and the sample.
  IV- After using the glass slide as a supporting plate, the etching of InP and InGaAs was done.
  V- The FBG fiber is then attached to the other side of glass slide using the water solvable UV glue.

- It should be noted that we tried to put the minimum amount of glue since at the end the glue can put stress on the membrane. We found out that the best way of putting the minimum amount of glue is to use the tip of bare fiber. It is even much better that dispenser. Photo of the sample after putting glue and applying UV from the top of the glass slide is shown in Figure 44.

Figure 44. photo of the sample after a glass slide with glue was placed on top of it.

- Photo of the backside after backside etching is shown below (Figure 45). It is evident that the membrane curled up and broke at some parts. We think that either the residual stress within the grown structure and the silicon oxide layer or the stress caused by the glue is responsible for this. But at least it showed us that this method at its simplest form doesn't work out properly.
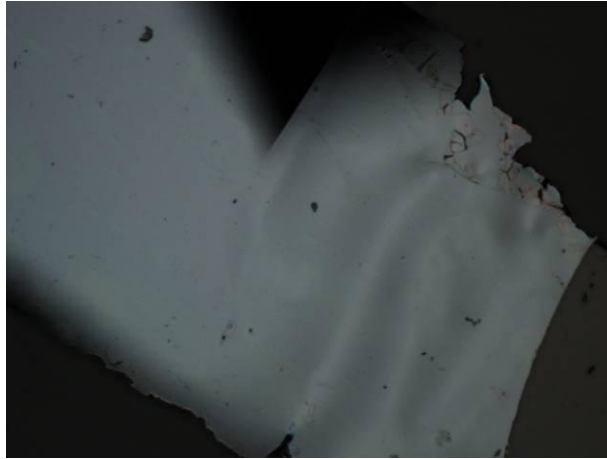

Figure 45. backside of the sample after complete removal of the substrate with pure Hcl.

- However we sent the best sample that was etched from backside and as shown in Figure 46 for PL measurements. This sample is still not good for the purpose of measurement with laser because it has been curled up near the edges (dark regions) and the laser cannot be focused into the ridges. However it is good for the purpose of checking the PL when the sample is etched up to the cladding layers. The PL which has been obtained by top illumination using a 900 nm laser beam at two different powers is shown in Figure 47.
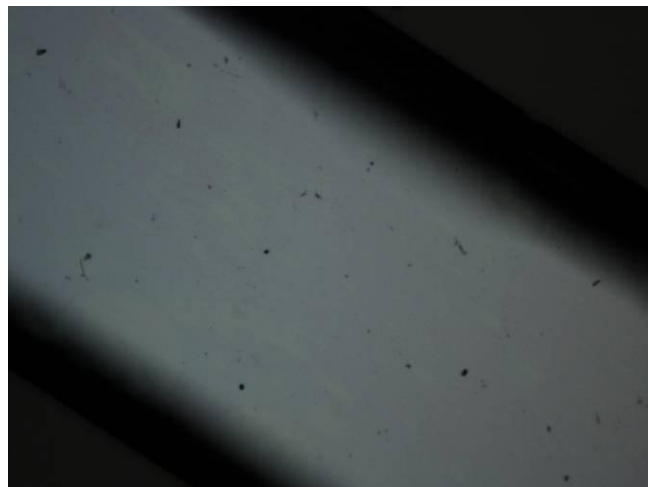

Figure 46. backside of the sample used for PL measurement after substrate removal.

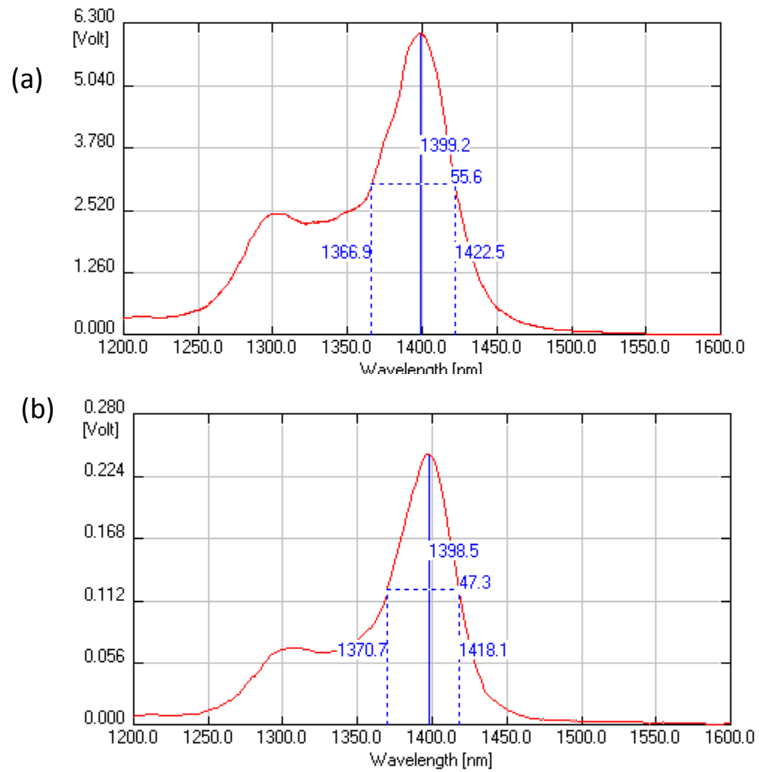**Figure 47, PL spectra of the the etched sample excited with a) a laser beam of 50 mW with a wavelength of 900 nm b) a laser beam of 2 mW at 900 nm.**

- The PL results have been shown in Figure 47 for two different powers. It is interesting to point out several differences of this PL to the PL of the full structure. First, the sample was a part of wafer that was previously known to have a PL peak at 1376 nm. Now this peak has been redshifted to 1400 nm. Second there are two peaks separated from each other in the new sample which might be due to the strain effects. A shoulder at the highest excitation power can be barely seen which is also predicted by theoretical predictions.

- In order to solve the problem of curling, we thought of having grid on the backside in order to support the membrane as an infrastructure. In order to do that we had to do a lithography on the backside.

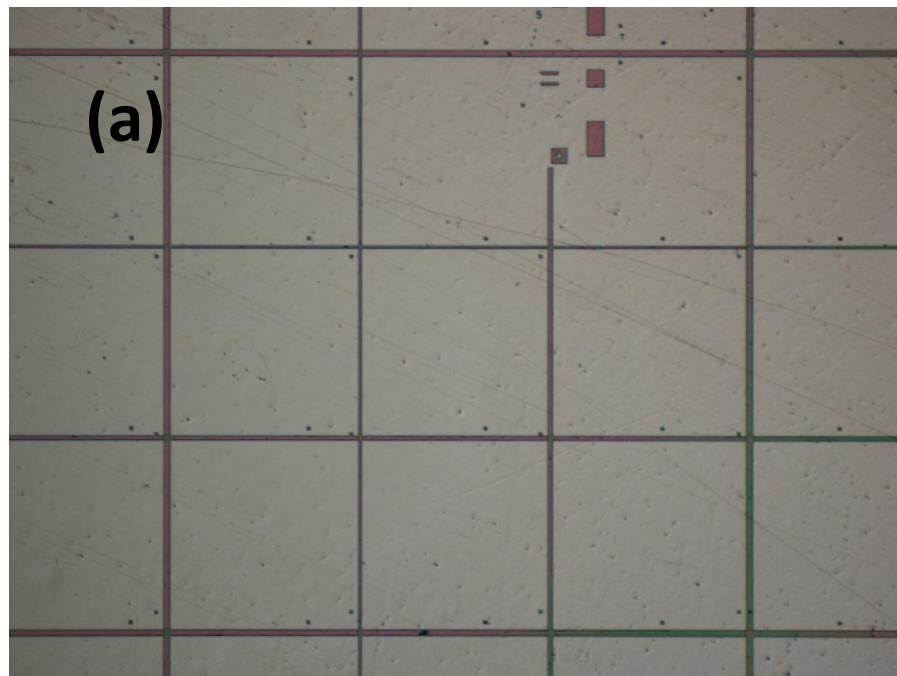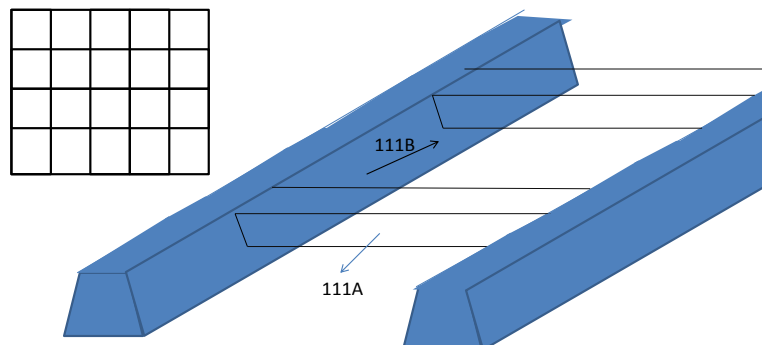- We first lapped and polished the sample from the backside to have a mirror-like surface suitable for lithography.

(a)

Figure 48 the fabricated grid on the backside.

- Since we didn't have a grid mask we used an opaque mask with ridge opening with the widths of 10 to 20 um. Then we did negative lithography twice to make the grids on the backside as shown in Figure 48.

- Then we put the sample into the etchant. According to the undercut and overcut directions we expected the final result to look like to the drawing shown in Figure 49.

- However after we put the sample into the etchant the bridges disappear after the etching. This might have been caused by the fact that after polishing a thin layer of an organi... ...ist to survive. We tried ... ...didn't survive. In that c... ...l the photoresist to stick ... ...pic hydrobromic

"Characterization and modelling of the strain fields associated with InGaAs layers on V-grooved InP substrates" Gupta Journal of applied physics, 82 (12), 15 December 1997

111B

111A

- **Figure 49 3D view of the grid on the backside after doing the wet etching with Hcl. The undercut and overcut for different directions was determined according to Ref[31].**

etching after polishing or having silicon oxide or nitride on the backside as the mask for wet etching.

- For two reason we stopped continuing the backside etching process. First the thermal simulations showed that the thermal resistance of the active region under the ridge to the rest of material is still too low for a Fiber Bragg grating to measure small changes of the temperature. Second the membrane without the substrate is very fragile and difficult to handle. Therefore we proceeded to use the suspended waveguide idea.
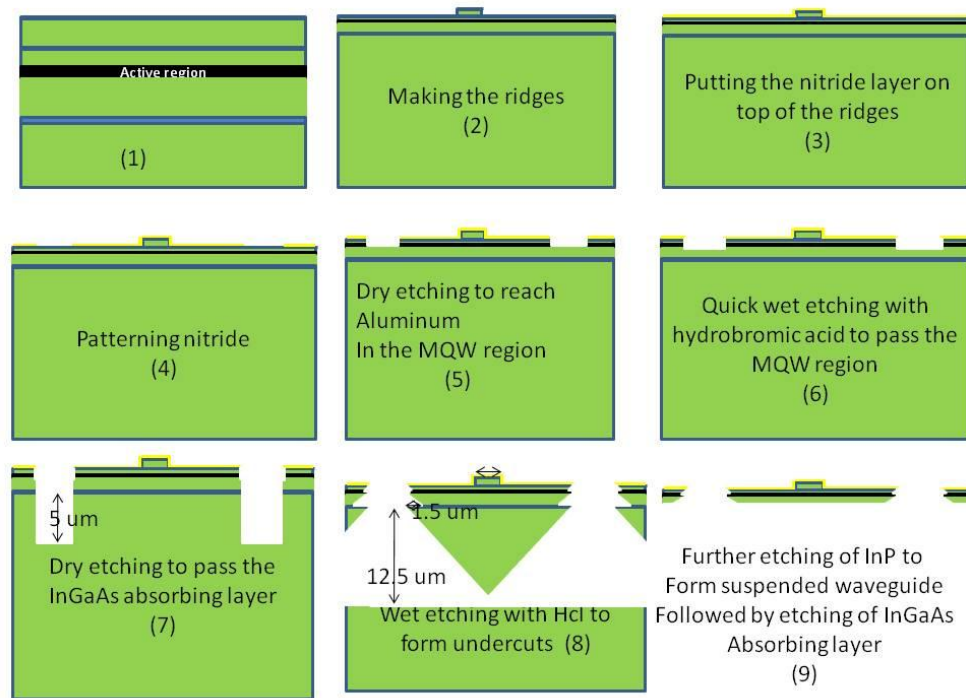
Suspended waveguide:

- Suspended waveguides on InP substrates have been fabricated by few groups [32,33]. In the previous efforts to make suspended waveguides, the general idea was to use an epitaxial thick sacrificial layer and etch it with a very selective etchant to release the structure. The suspended waveguides offer a lot of advantages such as reducing the substrate free carrier absorption[33], enhancing electro optic effect[32], etc but for demonstration of laser cooling they are specially distinctive: they provide very good thermal isolation from the surroundings as well as providing a very low thermal mass for the active region. These properties enable us to have very high thermal sensitivities so that even cooling and heating powers as low as 1 µW can be detected. Furthermore the carrier density can be made arbitrarily large even with low absorption so there will be no limitation imposed by maximum power that the laser can provide.

- We for the first time demonstrated that waveguide can be fabricated even without using sacrificial layers.

- We first devised two techniques which can be used to make the suspended waveguides out of our grown wafers. The schematics of the first and the second method are shown in Figure 50 Figure 51 . The process flow was as follows:

The process follow was as follows for the ridges fabricated along the dovetail direction (perpendicular to the major flat of the InP wafer):

1- Deposition of stress free silicon nitride layer.
2- Patterning the silicon nitride layer to form via holes.
3- Etching with RIE to reach the InAlAs layer in the MQW.
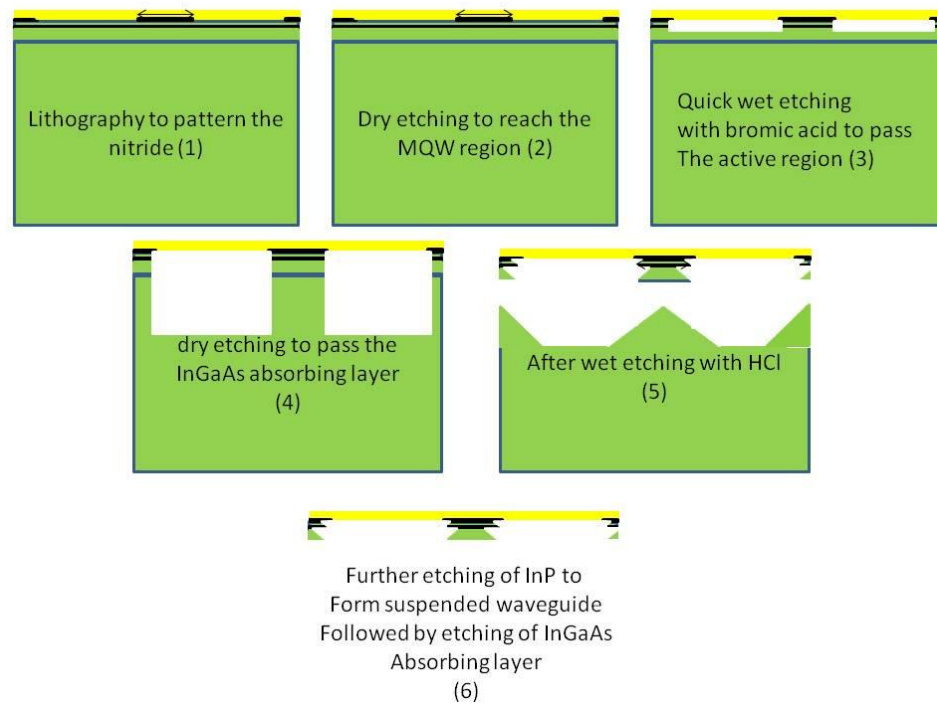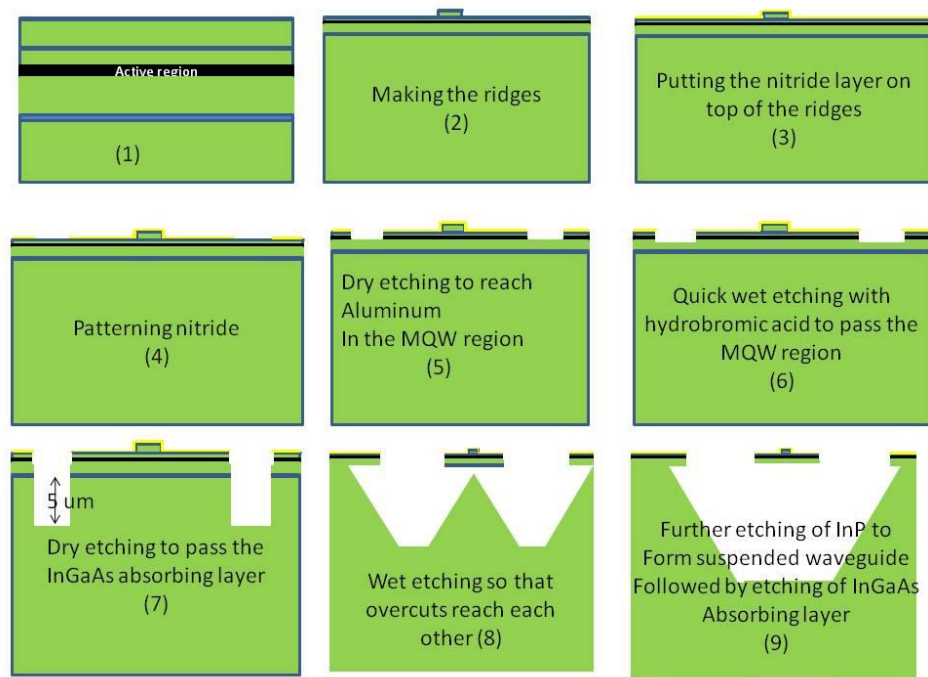
(a)

(b)

Figure 50. a) cross section b) side view of the process flow of making the suspended waveguide when the ridges are fabricated along the dove tail direction.
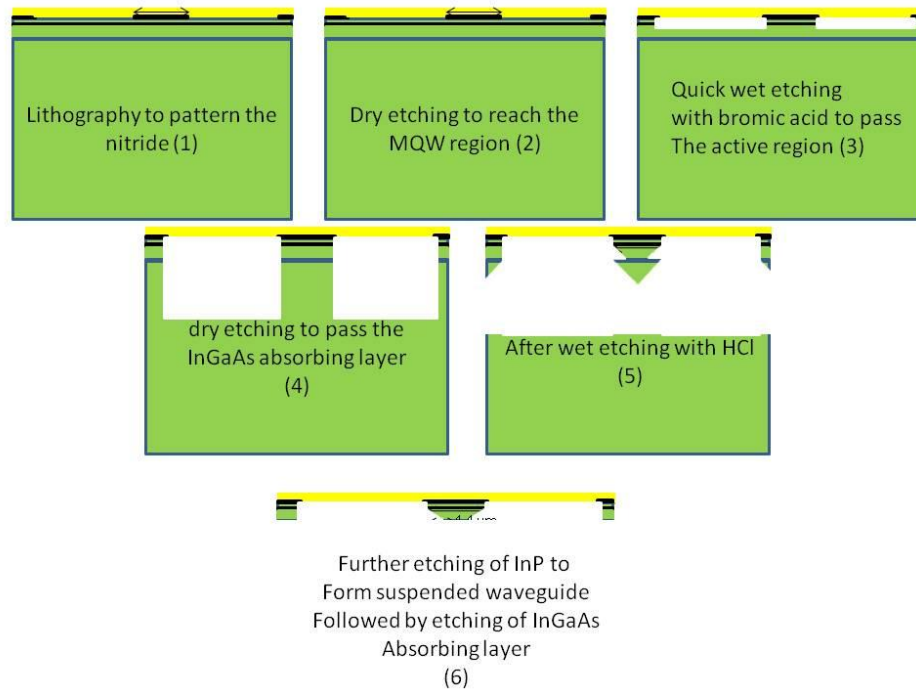
(a)

(1) Active region

Making the ridges (2)

Putting the nitride layer on top of the ridges (3)

Patterning nitride (4)

Dry etching to reach Aluminum In the MQW region (5)

Quick wet etching with hydrobromic acid to pass the MQW region (6)

5 um
Dry etching to pass the InGaAs absorbing layer (7)

Wet etching so that overcuts reach each other (8)

Further etching of InP to Form suspended waveguide Followed by etching of InGaAs Absorbing layer (9)

(b)

Lithography to pattern the nitride (1)

Dry etching to reach the MQW region (2)

Quick wet etching with bromic acid to pass The active region (3)

dry etching to pass the InGaAs absorbing layer (4)

After wet etching with HCl (5)

Further etching of InP to Form suspended waveguide Followed by etching of InGaAs Absorbing layer (6)

Figure 51. a) cross section b) side view of the process flow of making the suspended waveguide when the ridges are fabricated perpendicular to the dove tail direction.

4- Quick wet etching with hydrobromic acid to pass the MQW region.
5- Deep dry etching with RIE to pass the absorbing InGaAs layer.
6- Doing the wet etching with hydrochloric acid so that the undercuts under the waveguide and the overcuts under the small bridges reach each other and the suspended waveguide is released.
7- Further wet etching to reach the absorbing InGaAs layer from the bottom and then using selective etchant for InGaAs to remove the absorbing InGaAs layer.

The same process flow applies for the direction perpendicular to dove tail except that the overcuts form under the waveguide and the undercuts form under the small bridges.

- In order to test these ideas before doing the whole processing, we cleaved one test piece out of the wafer and did the first six steps using a suitable mask. According to the SEM photo as shown in Figure 52 , we found out that the overcuts never reach each other.

- Based on this conclusion we needed to change the process flow. First we have to make the ridges along the dovetail direction. Second we release the small bridges using hydrobromic acid which is an isotropic etchant and then we put the structure into hydrochloric acid so that the undercuts after complete etching reach each other under the waveguide and the micro machined structure gets suspended.
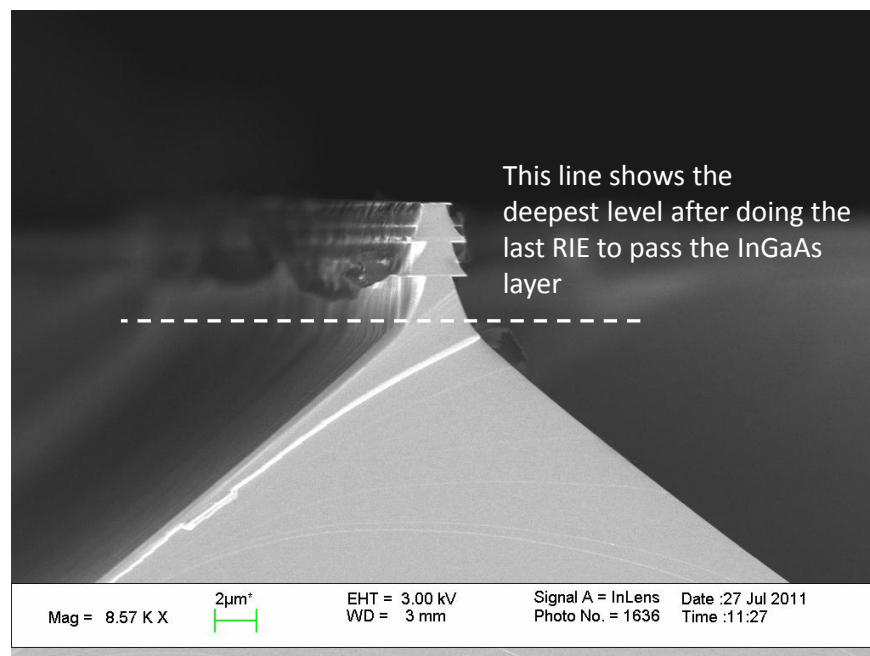

Figure 52. SEM photo of the test sample after doing the processing steps describes in the text.

- Before ordering the mask, we tested the new process flow and we were successful in making a suspended structure. Therefore we started to design and order the new mask.

- Before ordering the mask, a thermal simulation code was written and thermal simulation of the device was done in order to give us the temperature change of the device for a given thermal power. This is the temperature sensitivity of the device and should be as large as possible in order to have a good temperature measurement.

- It is evident that by increasing the spacing between the small bridges and by making the bridges thinner and narrower the temperature sensitivity increases however the mechanical stability of the suspended waveguide decreases. Therefore two designs for the suspended waveguides were considered. One of them is called "Conservative" and the other one is called "Performance".

- The bridges of the conventional designs are thicker (6 um except for the bridges under metal layers which are 8 um). And they are not as sparse as performance design's bridges. They are 40 um apart and the length of the bridges is 20 um as shown in Figure 53. Our calculations showed that this structure has a high mechanical stability and results to a high fabrication yield.

- The bridges of the performance designs are thinner (4 um except for the bridges under metal layers which are 8 um). And they are not as sparse as performance design's bridges. They are 80 um apart and the length of the bridges is 40 um as shown in Figure 53. The thermal sensitivity of this structure is very high and the calculations show that if the bridges are made by 100 nm of stress free silicon nitride the temperature of a 2 mm performance suspended waveguide will change by 0.1 degrees for a 1 μW absorption of thermal power. Our thermometers are going to be equipped with low noise amplifier which will make them capable of measuring temperature changes as small as 0.1 degrees. The thermal sensitivity of the performance design is approximately six times higher than that of the conventional design however it's mechanical stability is lower.

- Lift off masks for both Nickel and Chromium were designed as shown in Figure 54 and Figure 55 . The width of the metal strips is 4 um, which is half of the width of the bridges used to hold them. Therefore even a misalignment of 2 microns is acceptable.
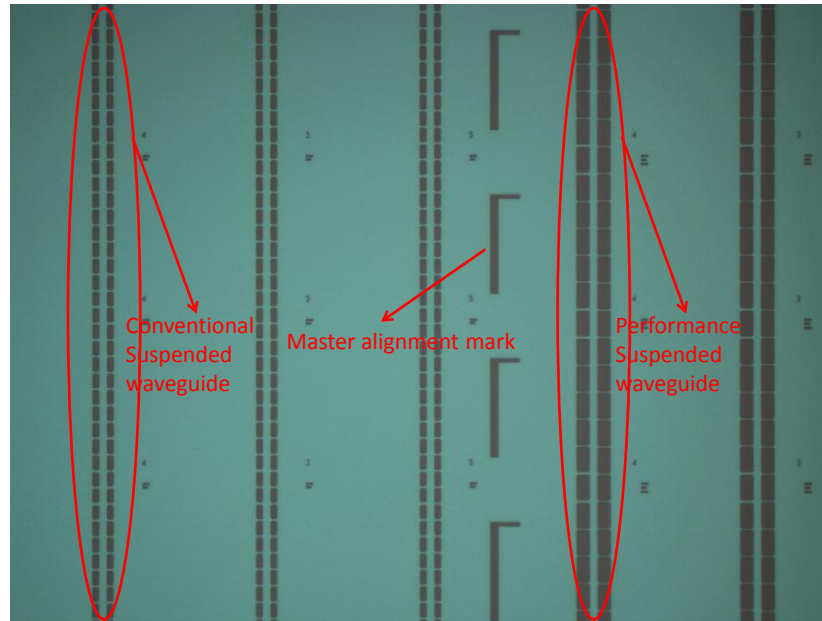
Figure 53 the Bridge mask containing transparent rectangles for making via holes. The conventional and the performance designs were also shown
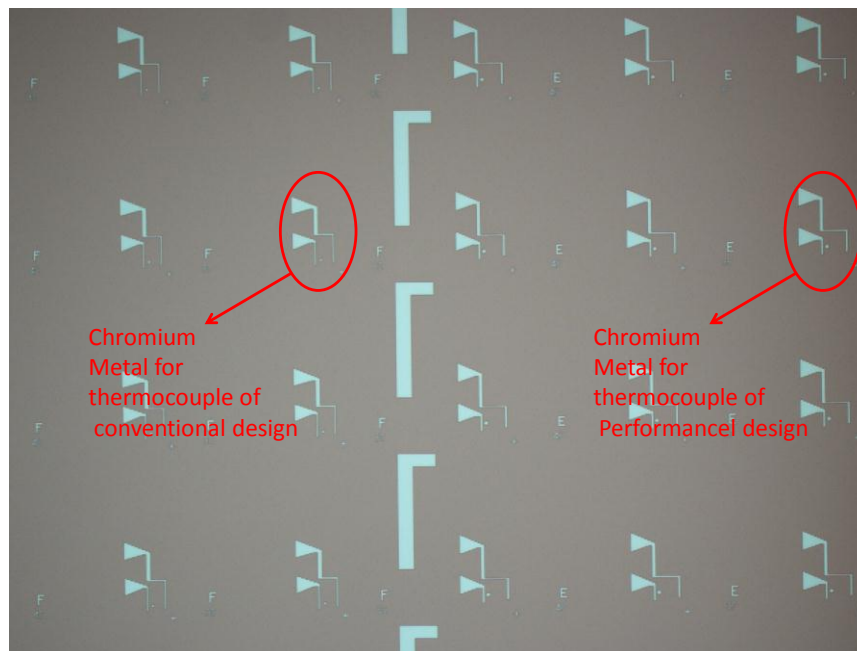

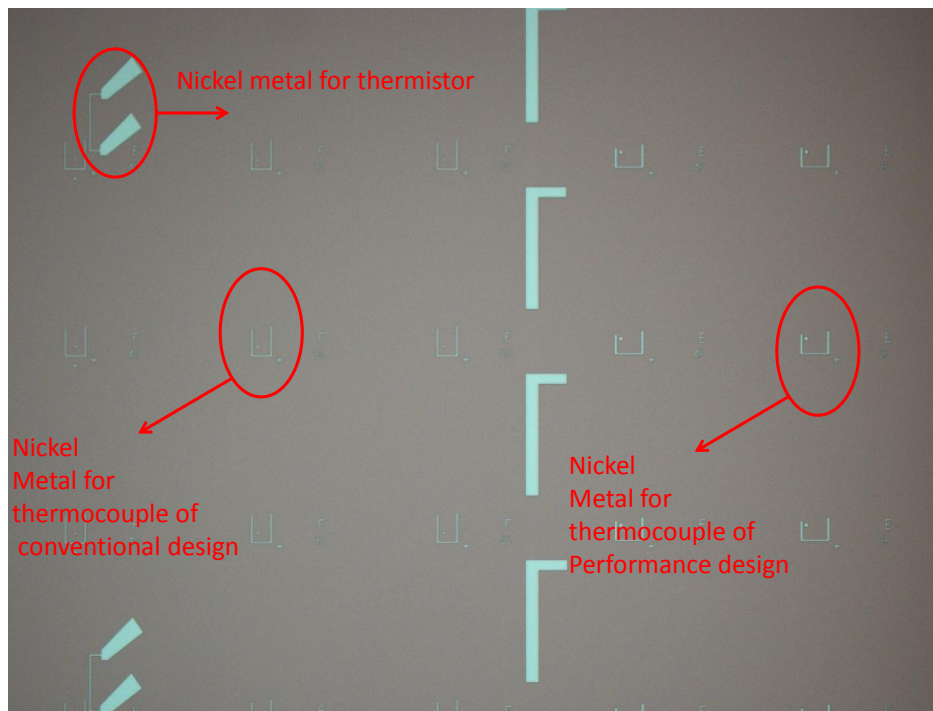**Figure 54. Lift off mask for chromium. The conservative and performance designs were also specified.**

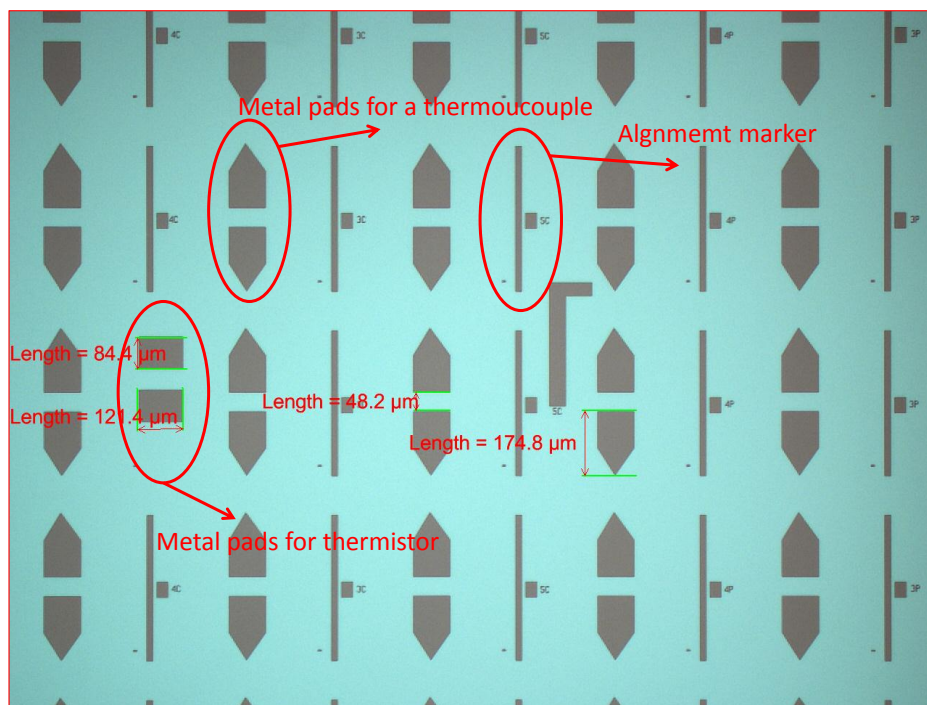**Figure 55. Lift off mask for chromium. The conservative and performance designs were also specified.**

Figure 56. contact mask which contains metal pads for wire bonding of both thermistors and thermocouples. The dimensions were also indicated.

- A mask for making metal pads was designed as shown in Figure 56. The arrows on the metal pads can help us to recognize the polarity of contacts easily if we want to make all thermocouples in series during the wire bonding. This mask is called "contact" mask.

- Subtle alignment markers were included on all of the masks to make the aligning of all five lithographies easier.

- The explanation of the final design putting all of the graduates the single printed in

Figure 57 a view of final device by putting all of the designs together. The thermistors and the thermocouples are also shown.

- The process flow for the sample and the mask set that we have is as follows:
  1-Making the ridges as described before.
  2- PECVD of Si_3N_4.
  3-Ti/Au lift off using the contact mask.
  4- O_2 plasma cleaning and removing the photoresist.
  5-Au seed layer sputtering.
  6- Photolithography with the contact mask.
  7- E_plating of Au.
  8-O_2 plasma cleaning and removing the photoresist.
  9- Au etching to remove the seed layer.
  10- Cr liftoff.
  13- Dipping in Hcl to remove the oxide from the surface of Cr.

14- Ni liftoff.

15- Patterning thick photoresist using the bridge opening mask.

17- Dry etching of Si_3N_4.

19- HBr etching, calibrated for the time needed for releasing of all bridges.

20- Hcl etching to form the suspended waveguide.

21- Photoresist removal.

23- Wire bonding.

24- Cleaving.

- In the first try we just used the bridge opening mask to make the suspended structure on the wafer. We were interested to see if both conservative and performance designs can survive.

- Fortunately both designed could be fabricated. After wet etching the last was to use the super critical drying.

- After supercritical drying, we tried to cleave the sample. Unfortunately they couldn't be cleaved well and most of the suspended waveguides broke. Therefore we investigated to see how we can solve the problem of cleaving.

- Finally two methods were tested for cleaving. In the first method just before doing the photolithography to make the bridge pattern, a PECVD stress free silicon nitride should be deposited. Then the silicon nitride should be patterned with bridge mask. Then a layer of silicon nitride should be deposited on the back and side walls of the sample. This can be done by putting the sample upside down inside the PECVD chamber. Next a short dry etching of silicon nitride should be done to remove the silicon nitride layer near the edges on the front side. An additional lithography with contact mask is needed to open the metal pads. At this point the side walls and the facets of the waveguide are protected and the hydrobromic and hydrochloric etching can be done to make the suspended waveguide. We tried this method and took the SEM of the microstructure as shown in Figure 58. The SEM photo has been taken with an angle of 45 degrees with respect to facet.

- The profile of etching near the facet is very similar to hydrobromic etching profile especially near the deepest point of the valley. Furthermore there is an overcut etch stop layer with the well known angle of 35 degrees. In Fact the deepest point after hydrobromic etching becomes anchor point because of the nitride on the facet, therefore if the undercuts under the waveguide don't reach each other

before intersecting with this etch stop layer, the etching with hydrochloric acid stops and the InGaAs layer cannot be etched consequently. consequently either
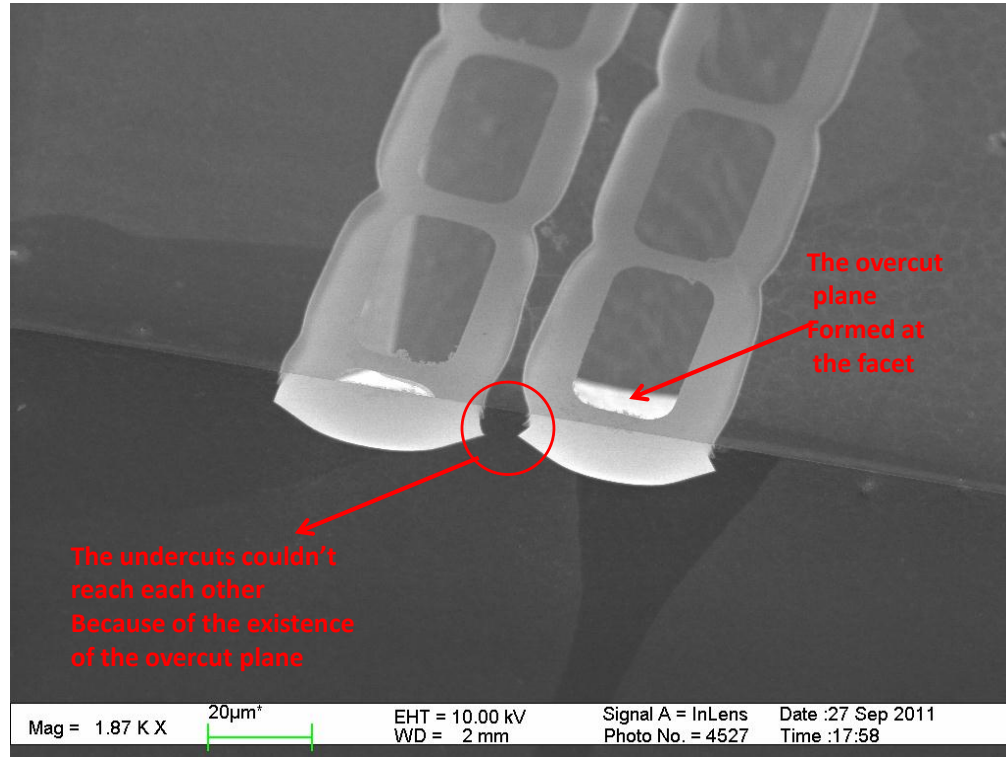

Figure 58 SEM photo of the suspend waveguide which was cleaved before Hcl etching and the side walls were protected using stress free silicon nitride. The overcut plane formed near the facet is also specified.

we need to do the dry etching to dig the substrate deep enough in order to provide enough depth for the undercuts to reach etch other or to use the crystal bond as explained in the next paragraph.

- Figure 58 shows that the etching profile of the hydrobromic acid is not even. Therefore the width of the suspended waveguide may change along the ridge. Although it changes gradually in practice and should not result to the scattering of the light propagating inside the ridge, but in order to see the maximum scattering due to a abrupt change of the waveguide width a mode simulation was done. Five layers have been considered, two of them air, two of them cladding and the core. For the first and second simulations the width of the cladding was considered to be 5 and 2.5 um respectively in order to find the scattering induced by change of the width of the cladding. The cross section of the core includes all of the layers listed in table 10.

Therefore first all of the layers of the grown wafer were put in a separate input structure and the effective index at 1.55 um using the transfer Matrix simulation code was calculated. For the cladding layers we did the same except that we exclude the layers within the ridge. The effective index of the core and cladding were calculated
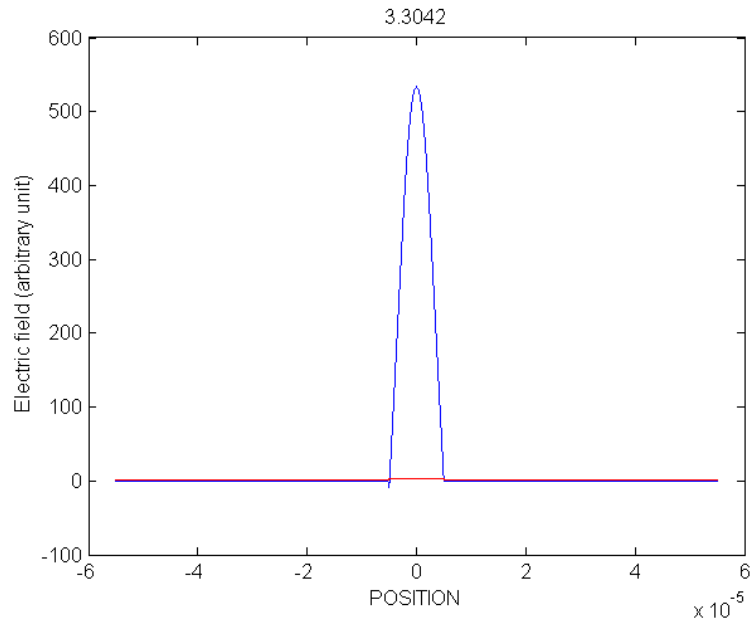
(a)

(b)
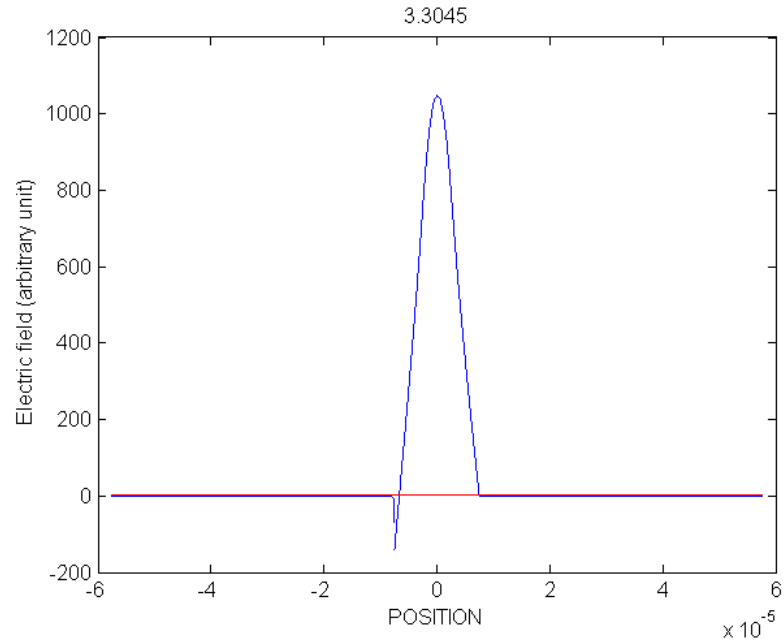
Figure 59 for 2.5 um cladding. Position is in units of meters.

The scattering coefficient will be:

to be 3.3053 and 3.3042, for the cladding of 5 um the effective index is calculated to be 3.3045 and for the cladding of 2.5 um it is calculated to be 3.3042 (see Figure 59 a,b)

$$R = \frac{(n_1 - n_2)^2}{(n_1 + n_2)^2} = 2 \times 10^{-9}$$

This is fortunately negligible. Therefore the hydrobromic etching profile is not a major issue.

- The other method of cleaving is to make the suspended waveguide and then cleaving it using the crystal bond. The melt crystal bond is first pushed toward one side of the sample. Then the crystal bond gets sucked by the capillary force into the micro channel under the suspended waveguide. The crystal bond supports the bridges during the cleavage. After cleaving the sample is put into the acetone to dissolve the crystal bond. The sample is then washed with running alcohol and transferred to a beaker of alcohol for super critical drying. This method doesn't need additional processing steps like the previous method which is beneficial since it ensures the metals used for
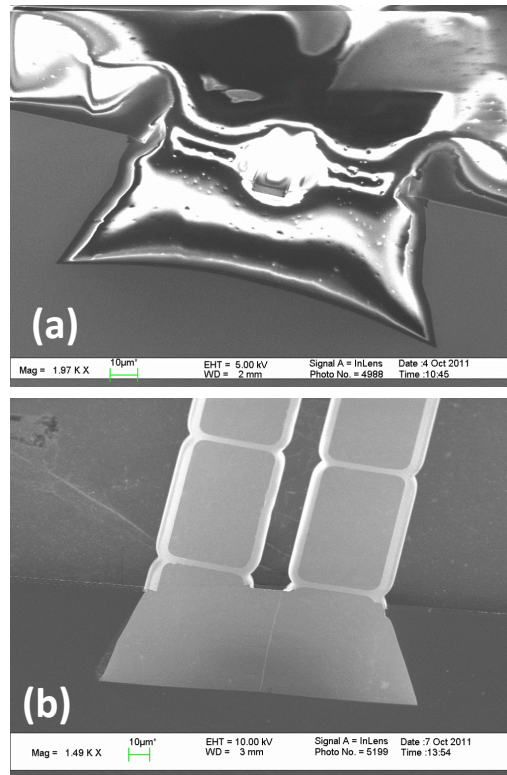

Figure 60. SEM cross section of a suspended waveguide which was filled with crystal bond and then cleaved. (a) sample with crystal bond (b) sample after removal of the crystal bond by acetone.

thermometry don't react with other chemicals to form unknown compounds at metal surfaces. Fortunately when we tested this method most of the suspended waveguides were cleaved nicely. Figure 60 shows one of facets which was cleaved using this method before and after the removal of the crystal bond.

- We followed all the steps based on our results and fabricated the device as shown in Figure 61. Unfortunately the thermistors didn't survive due to a problem of the mask. But we could use the thermocouples as described in the measurement section.
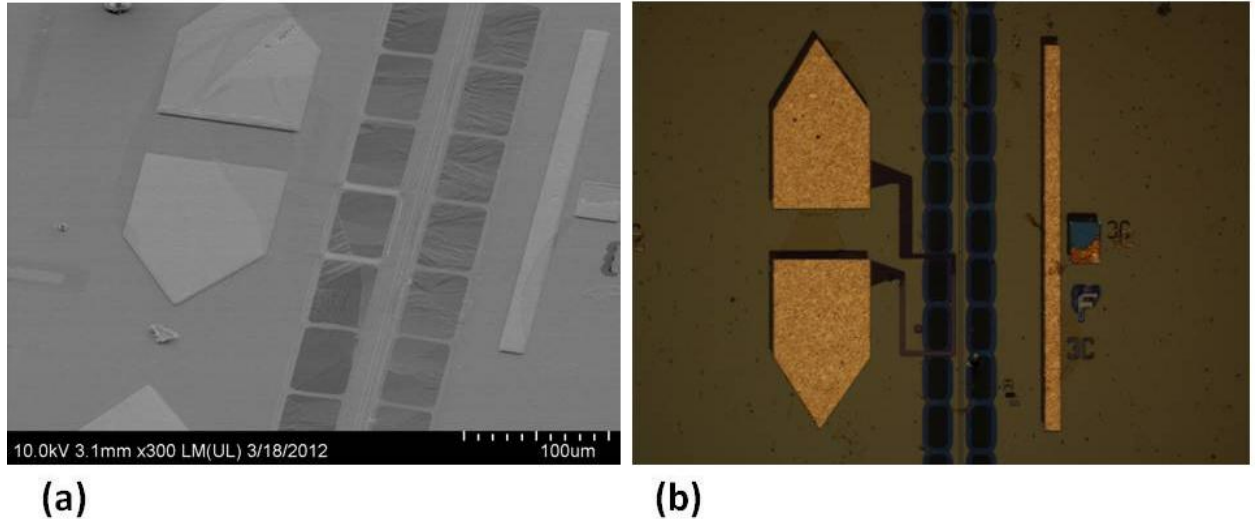

Figure 61 the fabricated suspended waveguide a) SEM photo b) optical image.

- Photon trapping happens when the PL cannot come out of the structure because of total internal reflection. It is the most important problem for laser cooling of semiconductors. In order to address this problem, we want to make gratings on the suspended device in future. The grating should be capable of coupling the pump beam which is focused on top of the grating into the waveguide and also should extract most of the PL out of the structure.

- Since the PL wavelength is near to 1550, we started by the design suggested by Taillaert et al [34]. The fabricated structures have a period of approximately 600 nm as shown in Figure 6261.
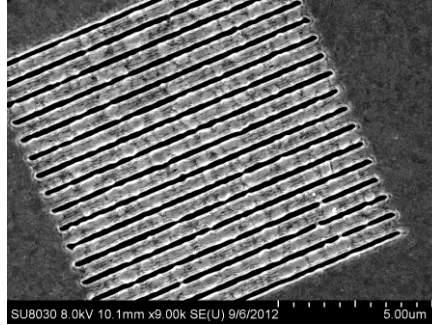
Figure 62 the SEM image of the grating fabricated using FIB.

- In order to fabricate the grating a test wafer was used with same MQW structure but its top cladding layer which is p-doped InP is only 100 nm thick. 50 nm of gold was deposited using e-beam evaporation. The gold was pattered using FIB and the grating was fabricated as shown in Figure **62**62.

Measurements

- First we aligned the laser using lenses from the side to couple the light into the ridge and collect the light from the output facet. Then we performed a wavelength scan and measured the output power as shown in Figure 63(a). Using the Fabry Perot theory and doing an FFT analysis we obtained the distribution of cavity lengths as shown in Figure 63(b). The cleaved sample was approximately 1.5 millimeters. This is evident in Figure 63(b) however the peak corresponding to that cavity length is very broad.
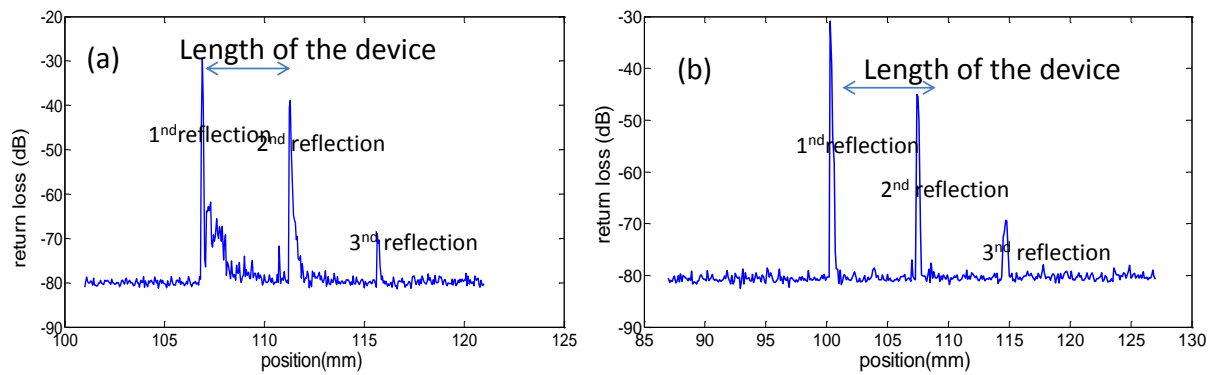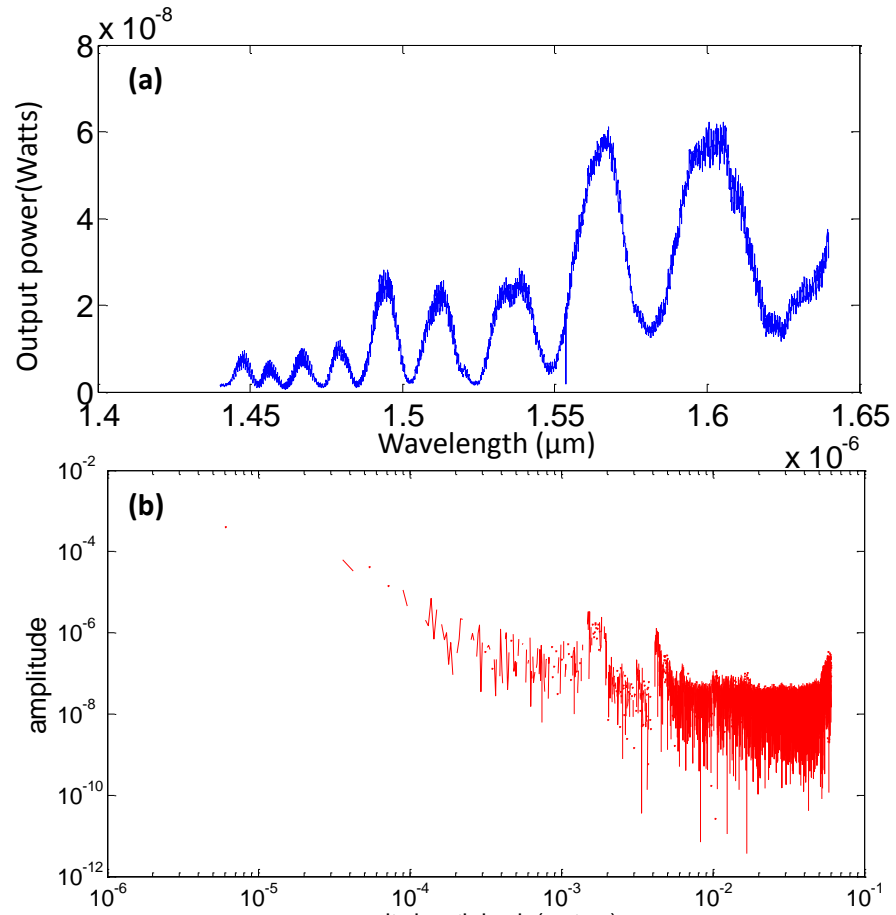
Figure 64 return loss versus position for (a) suspended waveguide (b) a single mode-non suspended waveguide.
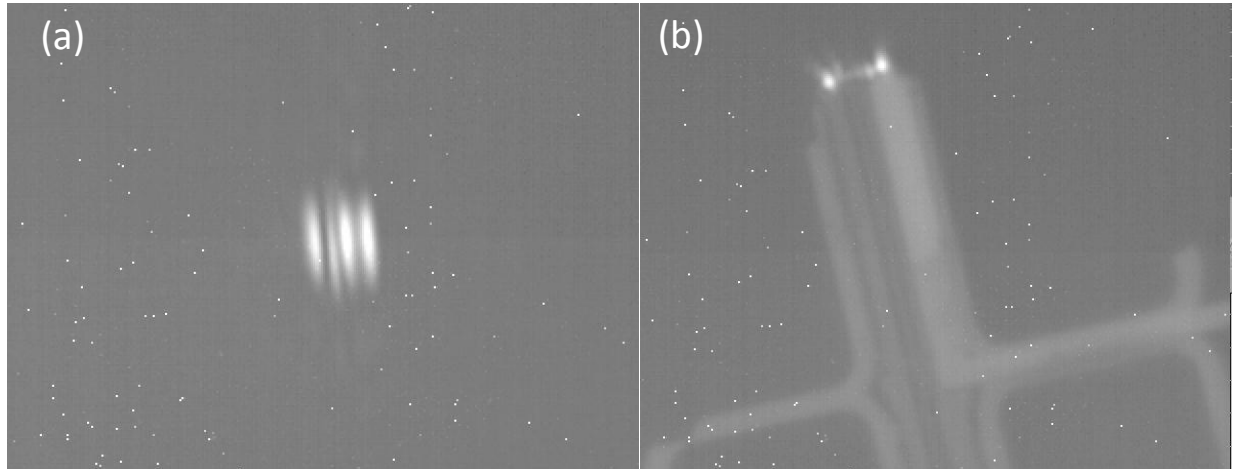
Figure 65 (a) front view (b) top view of the output facet of the suspended waveguide.

- In order to have a better understanding of the cavities inside the device, we used a high precision reflectometer (Agilent 8504B). The reflection versus position is shown in Figure 64. Compared to a non-suspended and single mode device fabricated on a different wafer, we don't see sharp peaks in this case and the reflection gradually decreases inside the device.

- The infrared images as shown in **Figure** 65 reveal that the waveguide is multi-moded and there is always more than one mode even with the best alignment to the ridge. This is the main reason behind the behavior of the reflection spectra since different optical modes have different indices of refraction and group velocity inside the material which makes the reflection amplitude distributed over the length.

- The presence of different optical modes inside the device makes the calculation of absorption coefficient extremely difficult using the Fabry Perot and the reflection method [35,36]. Therefore we decided to perform the optical measurements by focusing the laser from top on the surface of the sample. The measurement of optical absorption gives us guidelines for finding the best pump power and wavelength for the purpose of laser cooling.

- In the next step the temperature was measured using the thermocouple when the laser was modulated at 200 Hz and the output voltage of the thermocouple was measured using the Lock-in amplifier. It turned out that the temperature changes as small as 10^{-3} K can be measured.

- The laser was focused from the top and the temperature change was recorded. Both wavelength and power were scanned for TE and TM modes as shown in Figure 66. It is evident that the TE mode leads to a higher temperature change because its absorption is higher. It is really interesting that for both modes the temperature change is lower for lower wavelengths with higher absorption. This can be a signature of laser cooling at higher energies but we still suspect to the interferometric issues and suggest further investigations to examine the validity of our assumptions.
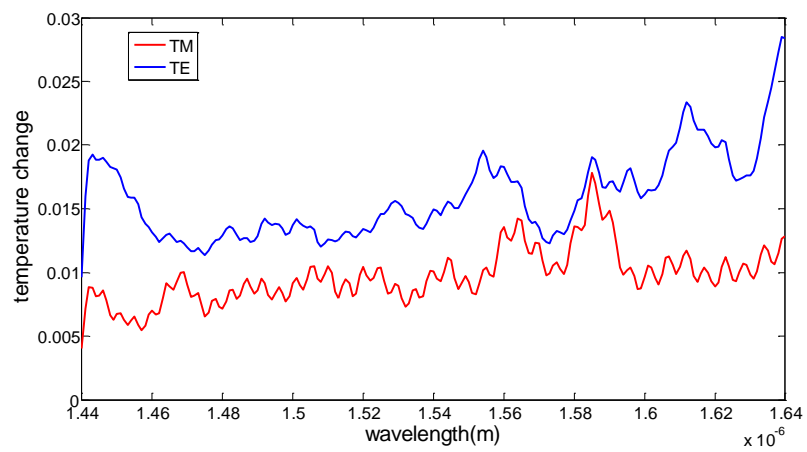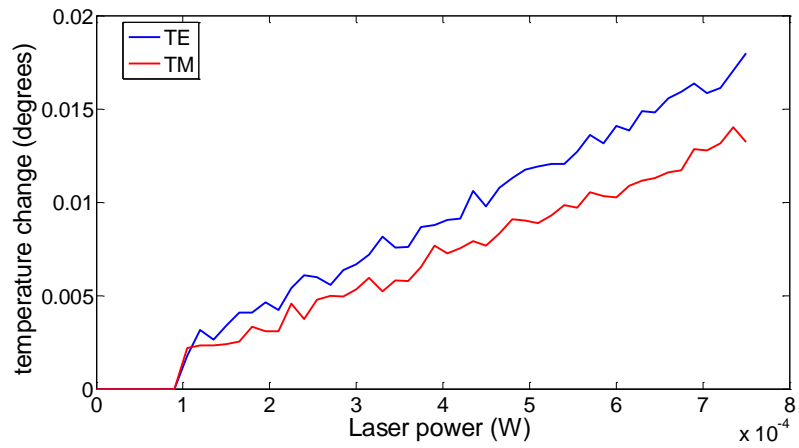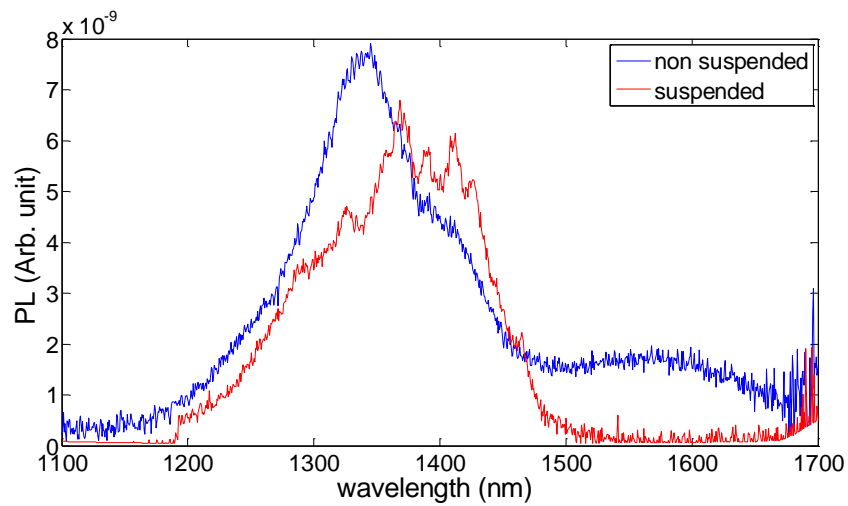
and TM modes

Figure 67 PL measurements for both suspended and non suspended part of the wafer.
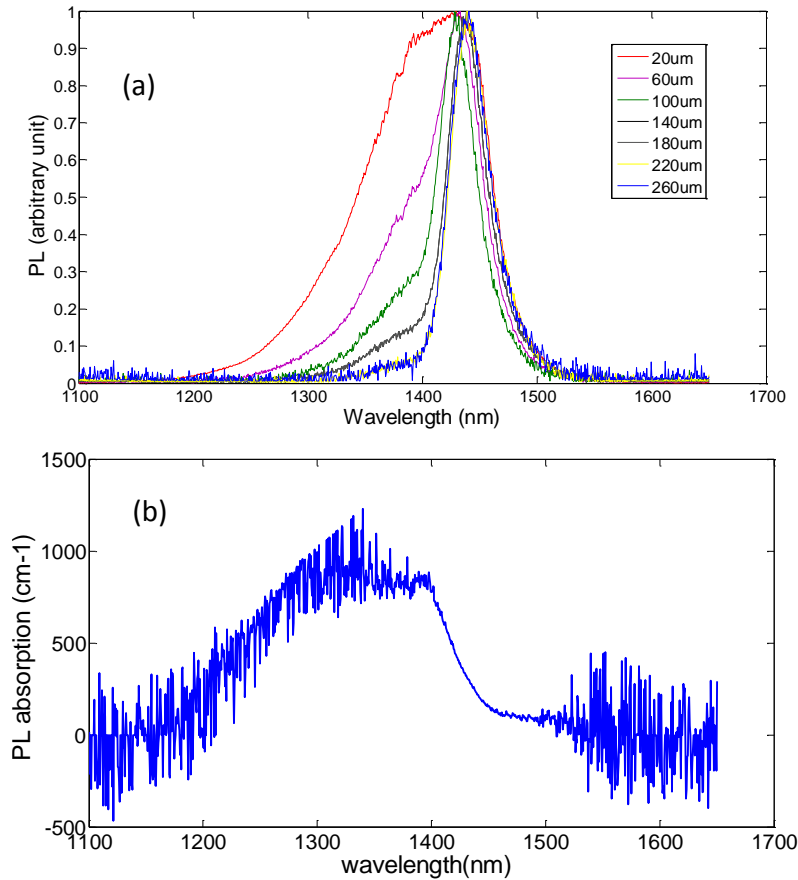
Figure 6861 (a) PL spectra for different distances of the pump laser spot with respect to the output facet of the waveguide (b) calculated reabsorption coefficient for PL calculated according the results obtained in (a).

- We developed our setup and used a 980 nm laser to measure the photoluminescence. The photoluminescence for both suspended and non suspended part of the wafer was measured and the result is shown in Figure 67 PL measurements for both suspended and non suspended part **of the wafer.** The photoluminescence of the suspended part is clearly redshifted and is broader. We later proved that this is due to the temperature rise in the suspended region. The temperature of the sample was increased to 200 centigrade and the PL of the non-suspended part excellently matched the PL of the suspended part at room temperature. The temperature rise of the suspended part at room temperature is attributed to thermal isolation.

- In order to find the reabsorption of PL along the waveguide which is known as photon recycling, the ridge waveguide was illuminated from top and the PL signal was detected from the side facet of the waveguide. The distance between the illumination and the side facet changed and the PL spectra was recorded (see Figure **6861**68). The higher energy side of the PL is damped heavily as the distance increases. The absorption spectra of the PL was calculated based on these results and is plotted in Figure **6861**68(b). In the regions with high noise the PL intensity was low and the reabsorption spectra shows large fluctuations.

- Lastly, in order to investigate the performance of the grating, an optical setup capable of obtaining the far-field images was designed and assembled. It is comprised of an inverted microscope and an upright microscope as shown in Figure 69. The sample is polished in order to allow the beam to enter the active region without scattering from backside using the inverted microscope. The upright microscope has the same structure as the inverted microscope and it is used for both collecting and imaging the beam coming of the grating structure. The far field image was obtained by removing the camera lens.

- The sample with grating as described in the fabrication section was polished from the backside and the beam was focused from the backside on the front side using the inverted microscope. The beam going out of the front surface goes into the top microscope for far-field imaging. In order to eliminate the interference of the beam reflected from the front surface, a low NA(~0.1) lens was used in the backside microscope with a tilted orientation.

- The far field and the near field images are shown in Figure 70. As you see the shift of far field is evident for the grating when the wavelength is changed by 200 nm around 1550 nm. This shift corresponds to the change of the angle of radiation and is caused by the grating. The shift of the beam corresponds to a certain angle of irradiation from the front surface.
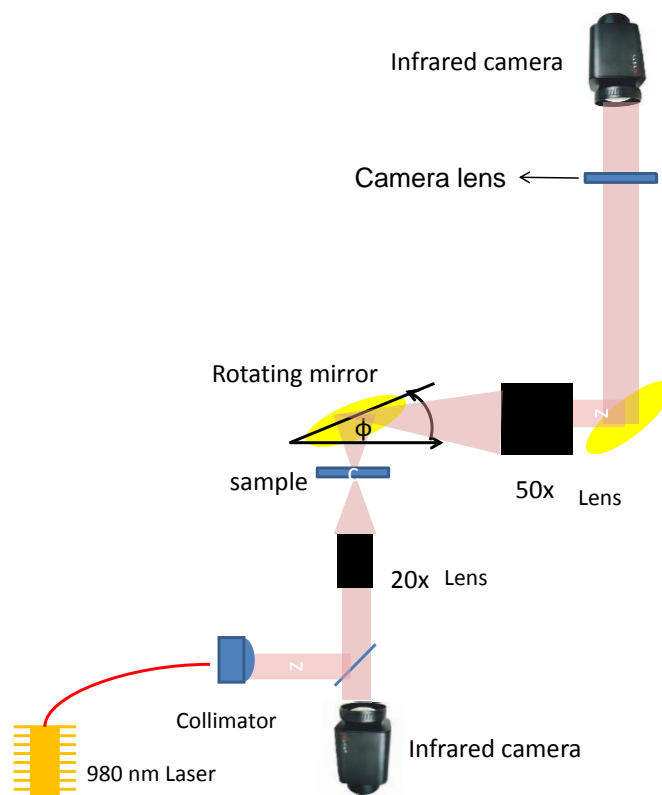
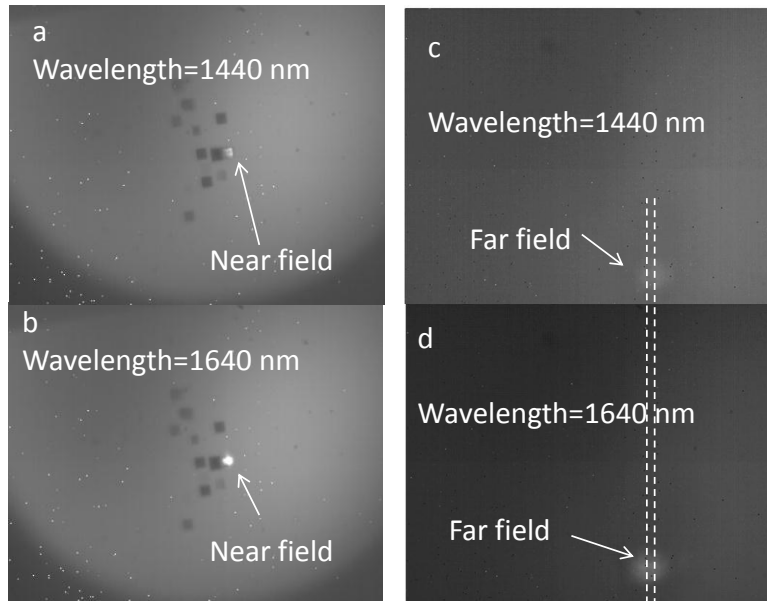**Figure 69 the setup for capturing the far field image of the beam**

Figure 70 a) near field image when the pump wavelength is 1440 nm (a) and 1640 nm (b). The far field image when the pump wavelength is 1440 nm (c) and 1640 nm (d). The shift of the far field peak is evident for two different wavelength and is specified by the dashed line.

- The near field images show different grating as rectangles next to each other. For the results given here only one of those gratings was used.

Conclusions and the suggested future:

- We could successfully fabricate the suspended device and removed the InGaAs absorbing layer.

- We obtained output power spectrum and reflection profile of the suspended waveguide. Those results together with the infrared image of the waveguide facet showed that the multimode nature of the suspended waveguide. This is the reason behind the complexity of the results.

- We fabricated thermocouples and measured the temperature with high accuracy (10^{-3} K). we also made a thermo reflectance system which is capable of showing the temperature map with the accuracy of 500 nm.

- We measured the temperature by scanning the wavelength and power of the laser.

- We developed the optical setup for PL measurements and obtained the PL spectra for both suspended and non suspended part. Based on the top illumination and side collection, the PL reabsorption coefficient was measured.

- In order to eliminate the interferometric effects of top illumination configuration, one can use a low NA lens and tilting the sample such that the reflected beam at the bottom semiconductor/air interface doesn't travel the same path back to the top surface. However at this point the surface of the sample cannot be seen by the microscope and the alignment of the beam and device becomes difficult.

- We suggest doing the excitation dependent PL using our setup in order to calculate the recombination coefficients then using the absorption spectra we can determine the range of powers and wavelengths which are more prone to cooling.

- The optical setup should be prepared such that the sample can be place inside a cryostat. As the temperature decreases the radiative recombination increases while the other recombination coefficients decrease which is favorable for laser cooling.

- For increasing the carrier density by top illumination, methods of carrier confinement should be investigated.

- We are planning to make the grating on the suspended waveguide and measure the out of plane coupling of the grating using by coupling the light coming out of the waveguide into a fiber. For this reason in the next step which is fabrication of the grating on the suspended waveguide, will be investigated and the out of plane coupling will be measured.

- Making different gratings with different directions near to each other will be also fruitful for studying the far field emission characteristics for the wavelengths of the interest.

References:

1 Epstein et al., "Observation of Laser-Induced Fluorescent Cooling of a Solid" Nature, 377, pp.500, 1995.

2 Ruan et al"Advances in Laser Cooling of Solids" J of Heat.Trans, 129, pp.3 2007.

3 Bahae "Advances in laser cooling of semiconductors" Proc. SPIE, 6115, pp. 611518 2006.

4 Gauck et al "External radiative quantum efficiency of 96% from a GaAs /GaInP heterostructure"Appl. Phys. A, 64, pp.143-147, 1997.

5 Imangholi et al "Effects of epitaxial lift-off on interface recombination and laser cooling in GaInP/GaAs heterostructures" Appl.Phys.Lett, 86, pp.081104, 2005.

6 Khurgin "Band gap engineering for laser cooling of semiconductors" Proc. SPIE, 6115, pp. 611519 2006.

7 D. Turchinovich et al "Role of dynamical screening in excitation kinetics of biased quantum wells: Nonlinear absorption and ultra broadband terahertz emission" J Applied Phys, 99, pp. 013510, 2006.

8 D. Turchinovich et al "Ultrafast polarization dynamics in biased quantum wells under strong femtosecond optical excitation", Phys Rev B, 68, pp.241307, 2003.

9   M Yamanishi, "Field-Induced Optical Nonlinearity Due to Virtual Transitions in Semiconductor Quantum-Well Structures" Phys. Rev. Lett, 59, pp.1014–1017, 1987.

10 D.S Chemla et al, "Generation of Ultrashort Electrical Pulses through Screening by Virtual Populations in Biased Quantum Wells" Phys. Rev. Lett. 59, pp.1018–1021 1987.

11 A. Shimizu "Photon-energy dissipation caused by an external electric circuit in ''virtual'' photoexcitation processes" Phys. Rev. Lett, 72, pp. 3343–3346, 1994.

12 W.H. Knox "Femtosecond ac Stark Effect in Semiconductor Quantum Wells:Extreme Low- and High-Intensity Limits." Phys. Rev. Lett, 62, pp.1189–1192 1989.

13 Van de Walle," band lineups and the deformation potentials in the model solid theory" Phys. Rev B, 39, pp.1871, 1989.

14 D. Marcuse "Reflection Loss of Laser Mode From Tilted End Mirror" J light Wave Tech,7, pp.336, 1989.

15 L. N. Kurbatov et al"Investigation of superluminescence emitted by a gallium arsenide diode," Sov. Phys. Semicond vol. 4.pp. 1739-1744, 1971.

16 Pabla et al., "Electroabsorption modulation in strained piezoelectric InGaAs/lnP multiquanturn wells operating at λ= 1.55 µm" IEEE Elec Lett., 30, pp.1707, 1994.

17 Sanchez-Rojas et al. "Dependence on the In concentration of the piezoelectric field in (111)B InGaAs/GaAs strained heterostructures" Appl. Phys. Lett., 65, pp.2042, 1994.

18 Peter et al. "Band gaps and band offsets in strained GaAs12ySby on InP grown by metalorganic chemical vapor deposition" Appl. Phys. Lett. 74, pp. 410, 1999.

19 Vurgaftman et al. "Band parameters for III–V compound semiconductors and their alloys" J. Appl.Phys., 89, pp. 5815, 2001.

20 Vurgaftman et al. "Band parameters for nitrogen-containing semiconductors" J. Appl. Phys., 94, pp.3675, 2003.

21 Chiu et al. "Molecular beam epitaxy of $GaSb_{0.5}As_{0.5}$ and $Al_xGa_{1-x}Sb_yAs_{1-y}$ lattice matched to InP"Appl. Phys. Lett., 46, pp.408, 1985.

22 Murgatroyd et al. "Observation of {111} ordering and [110] modulation in molecular beam epitaxial $GaAs_{1-y}Sb_y$ layers: Possible relationship to surface reconstruction occurring during layer growth" J. Appl. Phys. 67, pp.2310, 1990.

23 Wei et al. "Proposal for III-V ordered alloys with infrared band gaps" Appl. Phys. Lett., 58, pp.2684, 1991.

24 Vurgaftman et al "Characteristics of strained GaAs1−ySby (0.16 <y < 0.69) quantum wells onInP substrates" J of Physics D, 40, pp.7656, 2007.

25 Boccara et al "Sensitive photothermal deflection technique for measuring absorption in optically thin media" OPTICS LETT, 5(9), pp.377 1980.

26 Imangholi et al "Differential Luminescence Thermometry in Semiconductor Laser Cooling" Proc. of SPIE , 6115, pp. 61151, 2006.

27 Tessier et al "Thermoreflectance temperature imaging of integrated circuits: calibration technique and quantitative comparison with integrated sensors and simulations" J. Phys. D: Appl. Phys, 39, pp. 4159–4166, 2006.

28 Tessier et al "Measuring and predicting the thermoreflectance sensitivity as a function of wavelength on encapsulated materials" Rev Scientific inst, 74, pp.495, 2003.

29 T.M. Berlicki, "Thermoresistive thin film flow sensor" Active and Passive Elec. Comp., 13, pp. 161-173. 1989.

30 C. Waschke et al "Coherent submillimeter-wave emission from Bloch oscillations in a semiconductor superlattice" Phys. Rev. Lett. 70, pp.3319–3322 1993.

31 A Gupta et al "Characterization and modelling of the strain fields associated with InGaAs layers on V-grooved InP substrates" J Applied Phys, 82 , pp.6016,1997.

32 T. H. Stievater "Enhanced Electro-Optic Phase Shifts in Suspended Waveguides" Optics Express, 18, pp. 885-892, 2008.

33 A. Whaley et al "Observation of low optical overlap mode propagation in nanoscale indium phosphide membrane waveguides" Appl Phys. Lett, 90, pp.011114, 2007.

34 Taillaert D et al "An Out-of-Plane Grating Coupler for Efficient Butt-Coupling Between Compact Planar Waveguides and Single-Mode Fibers" IEEE J OF Quant Elects, 38, pp.949, 2002.

35 S Chen et al "Optical waveguide propagation loss measurement using multiple reflections method" Optics Comm, 256, pp.68, 2005.

36 H. Mohseni et al "High-Performance Optical Modulators Based on Stepped Quantum Wells" Proc. of SPIE , pp.6127, 2006.